

Full Length Article

Rapid and efficient antibacterial activity of Molybdenum-Tungsten oxide from n-n heterojunctions and localized surface plasmon resonance



Da Hyeon Shin^{a,1}, Sosan Hwang^{a,1}, Ye Seo Park^a, Jihyun Kim^b, Seojin Lee^c, Sanghyun Hong^c, Sang Eun Shim^{a,*}, Yingjie Qian^{a,*}

^a Department of Chemistry and Chemical Engineering, Education and Research Center for Smart Energy and Materials, Inha University, Incheon 22212, South Korea

^b Institute of Space and Technology Research Center, Inha University, Incheon 22212, South Korea

^c LG Electronics Inc. 51, Gasan digital 1-ro, Geumcheon-gu, Seoul 08592, South Korea

ARTICLE INFO

ABSTRACT

Keywords:

N-type semiconductor
 $\text{Mo}_{0.55}\text{W}_{0.45}\text{O}_{3-x}$
 Oxygen vacancy
 Reactive oxygen species
 UPS

With a surge in bacteria encroaching on our daily life, exacerbated antimicrobial resistance toward antibiotics, and sagacious short- and long-term responses of bacteria toward novel antibacterial nanoparticles, the need for developing rapid and effective antibacterial agents is increasing. Herein, $\text{Mo}_{0.55}\text{W}_{0.45}\text{O}_{3-x}$ samples are synthesized through a coprecipitation process, followed by annealing at 450–600 °C. $\text{Mo}_{0.55}\text{W}_{0.45}\text{O}_{3-x}$ samples showed outstanding activity after 10 min of incubation against *Staphylococcus aureus* (*S. aureus*) and *Escherichia coli* (*E. coli*) under the compact fluorescent lamp irradiation; the activities were 98.948 ± 1.890 and $98.413 \pm 1.080\%$ for *S. aureus* and *E. coli*, respectively. The role of each reactive oxygen species (ROS) in suppressing bacteria was studied. The strikingly fast antibacterial rate was discovered with respect to semiconducting features of $\text{Mo}_{0.55}\text{W}_{0.45}\text{O}_{3-x}$ samples, including band positions, trap state, and band gap. We found that well-formed n-n heterojunctions and localized surface plasmon resonance (LSPR) excitation are responsible for antibacterial performance. Accordingly, we believe that a band position-considered system with numerous n-n heterojunctions and LSPR excitation will lead to efficient generation and separation of electron-hole pairs, facilitating the generation of ROS and subsequently resulting in the enhanced antibacterial performance.

1. Introduction

The battle to stem the proliferation of bacteria and their encroachment on our daily life is ongoing. However, given emerging threats of the substantially increasing antimicrobial resistance [1,2], discovering and developing new antibacterials are urgent concerns [3,4]. Over the past years, three categories of artificial antibacterials have emerged in terms of pivotal components: metals, organics, and oxides [5,6]. Ag nanoparticles as one of the most widely studied metals have already been employed in various biomedical and antimicrobial technologies [7]. Similarly, Au-containing nanocomposites have also proved effective in sterilization [8]. Unfortunately, the paucity of their reserves and the recent discoveries of bacterial resistance mechanisms against Ag jeopardize their future use [9]. In addition, organic antibacterials due to their covalent features require careful consideration because of some limitations, such as lack of durability and stability and limited operating pH range. Oxides, however, are promising and could be efficacious

against bacteria because the Earth is rich in diverse minerals for producing myriad cost-effective and robust oxides. A few of which have already demonstrated their effectiveness as antibacterials [10–12].

Over the past four decades, ZnO [10], FeO_x [11], TiO₂ [12], among others, have been extensively studied by considering factors such as the surface charge, shape, and concentration of nanomaterials; dispersion and contact between nanomaterials and bacterial cells; the presence of reactive oxygen species (ROS); release of metal ions, medium composition, and pH; specific surface area to volume ratio; and size. Among these factors, surface charge, release of metal ions, and production of ROS are critical in realizing antimicrobials with excellent performance. Currently, diverse attempts at containing bacteria are being conducted, including constructing binary or ternary ZnO-based materials to produce more electron-hole pairs [13,14], introducing phosphorus and fluorine to TiO₂ to maximize photocatalytic activity [15], and incorporating magnetic FeO_x to kill bacteria [16]. Concurrently, bacteria are evolving survival mechanisms that are beyond our comprehension: 1)

* Corresponding authors.

E-mail addresses: seshim@inha.ac.kr (S. Eun Shim), yjqian@inha.ac.kr (Y. Qian).

¹ These authors contributed equally to this work.

Envelope stress responses protect bacteria from contact with positively charged [17] or negatively charged nanoparticles [18]. 2) The efflux system expressed in metal resistance genes mediates the efflux of Zn^{2+} , Co^{2+} , Ni^{2+} , Fe^{2+} , Cu^{+} , H^+ , etc., from bacteria [19,20]. 3) Even more discouraging response is that ROS stimulate the activation of defense mechanisms in bacteria in short-term responses, i.e., activation of ROS scavenger enzymes [21,22], and in long-term responses, i.e., transcriptional level [23]—ROS inducing upregulation of antioxidant production within hours to days—and genomic level [24]—ROS causing damage and activating a DNA damage repair mechanism.

We do not have to be compelled to choose the lesser of the two evils—facing genetic mutation, long-term exposure, or compromising on antibacterial efficiency, short-term exposure. We can focus on understanding the profound nature of the antibacterial mechanism to fend off the attack instead of merely detecting ROS. There is still an undeniable gap between possible effective oxides and proved oxides previously described regarding a huge pool with promising semiconducting features. Therefore, the role of the band gap (E_g), band positions, or vacancies, as well as their influence on the generation of ROS should be elucidated to realize efficacious antibacterials. In 2012, Li et al. examined the antibacterial performance of several oxides, including TiO_2 , CeO_2 , ZnO , CuO , SiO_2 , Al_2O_3 , and Fe_2O_3 , and demonstrated a correlation between conduction and valence bands and ROS generation [25]. Moreover, recently reported studies including visible-light-driven nanosized 2D FeO_x [26] and band-engineered $H-TiO_{2-x}@\text{MOF}$ with oxygen vacancies [27] have substantiated the potential of semiconducting oxides in preventing the proliferation of bacteria. Studies on E_g , absorption, and photoluminescence proved that a larger E_g does not always preclude a weaker incident irradiation [28–30]. Instead, wide range of photo absorption, efficient electron-hole generation and separation, and retarded recombination are critical in improving photo efficiency as well as corresponding ROS generation [30]. In addition, localized surface plasmon resonance (LSPR) excitation [28–30] extends the spectral range of light absorption from visible to near-infrared for semiconducting oxides. Recent studies demonstrated that WO_{3-x} [31], MoO_{3-x} [30,32], and MoO_{3-x}/WO_{3-x} [33] are promising oxides owing to the presence of oxygen vacancies and LSPR excitation, resulting in faster charge kinetics or photocatalytic performances.

Previous studies suggest that MoO_{3-x}/WO_{3-x} is a promising candidate for fast and efficient disinfecting, especially when coupled with photon energy. Herein, $Mo_{0.55}W_{0.45}O_{3-x}$ samples with oxygen vacancies produced by thermal annealing were prepared, and their antibacterial performance was evaluated under weak incident light (compact fluorescent lamp: DULUX L 32 W, white, near 100 lx at 1 m) and under dark conditions for comparison. Surprisingly, after 10 min of incubation, 98.948 ± 1.890 and $98.413 \pm 1.080\%$ reductions of gram-positive and gram-negative bacteria under light conditions were observed, respectively, whereas 17.393 ± 4.454 and $20.134 \pm 4.002\%$ reductions of gram-positive and gram-negative bacteria were observed under dark conditions, respectively. The role of ROS in killing bacteria was specifically determined: $\bullet OH$ and O_2^- are effective ROS to kill bacteria whereas 1O_2 has no discernable effect on killing bacteria. In addition, the mechanism was elucidated by confirming the oxygen vacancy, work function (ϕ), E_g , electron affinity (EA), positions of the conduction band (E_C), Fermi level (E_F), and valence band (E_V) via X-ray photoelectron spectroscopy (XPS), ultraviolet-visible spectrophotometry (UV-Vis), and ultraviolet photoelectron spectroscopy (UPS) analyses. By combining antibacterial performance and band features of prepared samples, LSPR effect and well-formed E_{trap} proved to be essential factors to accomplish the fast and efficient antibacterial performance. We hope this work will set a precedent for and elucidate semiconducting oxide-based nanocomposites with fast, pragmatic, and cost-effective antimicrobial properties.

2. Experimental

2.1. Materials

MoO_3 ($\geq 99.5\%$), WO_3 , nitric acid (HNO_3 , 60%), and ethanol (EtOH, 99.5%) were supplied by Samchun Chemical (South Korea). Tetramethylammonium hydroxide (TMAH, 25% in H_2O), coumarin ($\geq 99\%$, HPLC), 1,3-diphenylisobenzofuran (DPBF, 97%), hydroxylamine hydrochloride ($NH_2OH-HCl$, 99%), iron (III) chloride ($FeCl_3$, 97%), and 1,10-phenanthroline ($\geq 99\%$) was obtained from Sigma-Aldrich (USA). The reagents were of analytical grade and were used without further purification. Deionized (DI) water was used.

2.2. Synthesis of $Mo_{0.55}W_{0.45}O_3$ nanoparticles

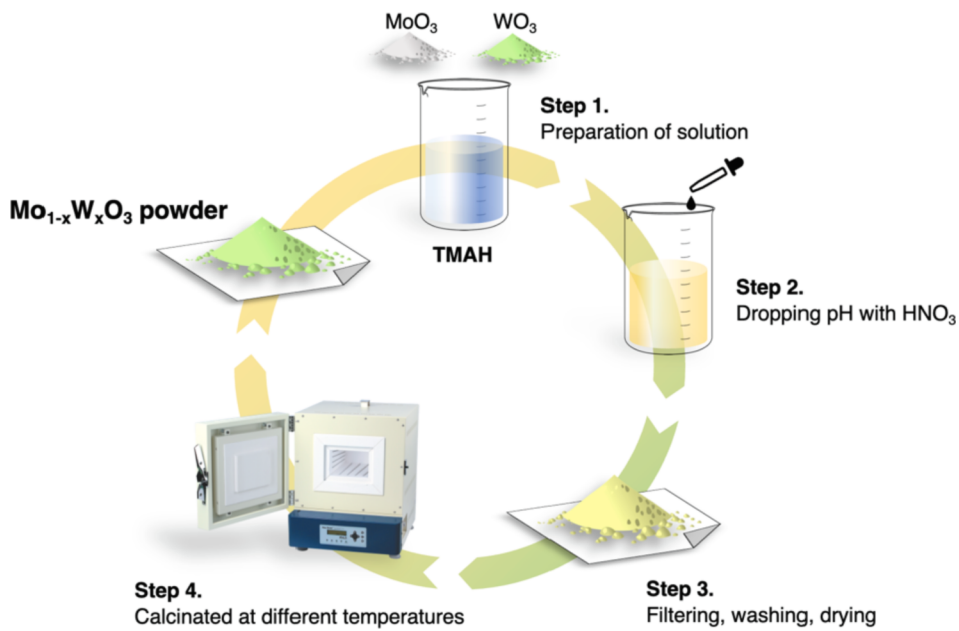
The overall preparation of $Mo_{0.55}W_{0.45}O_3$ sample is illustrated in Scheme 1. First, stoichiometric quantities of MoO_3 and WO_3 were added to 100 ml of 10 wt% aqueous TMAH solution, and the mixture was vigorously stirred at 60 °C for 1 h. After complete dissolution, the basic solution was added dropwise with nitric acid under constant stirring at 60 °C. The yellow precipitate was collected and washed several times with distilled DI water and EtOH. It was then dried at room temperature under a vacuum for 24 h. The dried yellow powder was kept in a muffle furnace and calcinated at different annealing temperatures (450, 500, 550, and 600 °C) in air for 1 h.

2.3. Characterization

The morphology of the as-prepared $Mo_{0.55}W_{0.45}O_3$ samples was analyzed using field emission scanning electron microscopy (FE-SEM, S-4300, Hitachi, Japan). The energy dispersive X-ray analysis (EDX) of the same particles was also performed using the same FE-SEM instrument. The crystallinity and phase were confirmed by X-ray diffraction (XRD, Rigaku, Japan) using an 18 kW Cu target range of 10–80°. High-resolution micrographs of the particles were obtained by transmission electron microscopy (TEM, JEM2100F, JEOL, Japan). The selected area electron diffraction pattern was also measured using the same TEM instrument. Elemental mapping was conducted under a high-angle annular bright-field mode and using an EDAX detector. The particle size distribution was measured using a zeta-potential and particle size analyzer (ELS-Z-2000, Otsuka, Japan). The Brunauer–Emmett–Teller (BET) surface area (S_{BET}) was measured by N_2 adsorption–desorption isotherms at 77 K (BELSORP-max, MicrotracBEL, Japan). Samples were dried under N_2 at 130 °C for 12 h before the BET analysis. The material composition and oxidation states of C, Mo, W, and O were analyzed using XPS (K-alpha, Thermo Scientific). The binding energies were calibrated to the 1 s peak (284.8 eV) of surface adventitious C. The UV–Vis absorbance spectra were recorded using a LAMBDA 950 UV/Vis/NIR spectrophotometer (PerkinElmer, USA). Photoluminescence spectra were measured with a fluorescence spectrophotometer (Shimadzu, Model RF-6000, Japan) equipped with a PC recorder. UPS characterization was performed on a PHI 5000 Versa Probe (ULVAC PHI, Japan) X-ray photoelectron spectroscope. The pH meter (HI2210, Hanna Instruments, USA) was first calibrated using appropriate buffer solutions (pH = 4.0, 7.0, and 10.0). The sample was thoroughly mixed in DI water at 10 mg/ml, and the pH was measured every 5 min. Compact fluorescent lamp (32 W, white) was purchased from DULUX L.

2.4. Antimicrobial property test

The antimicrobial activity of the samples was tested against gram-positive bacteria, *Staphylococcus aureus* (*S. aureus*) ATCC 6538, and gram-negative bacteria *Escherichia coli* (*E. coli*) ATCC 8739. The antibacterial effects of the fabricated materials were assessed using two different techniques to establish their efficacy at different annealing temperatures. The ability of the antibacterial agent to inhibit bacterial



Scheme 1. Schematic of preparation process of $\text{Mo}_{0.55}\text{W}_{0.45}\text{O}_3$ samples.

growth was first tested using a minimum inhibitory concentration (MIC) test. The shake-flask method using saline as a medium was also used to evaluate the antimicrobial efficacy of the fabricated nanoparticles.

2.4.1. MIC test

The MIC of $\text{Mo}_{0.55}\text{W}_{0.45}\text{O}_{3-x}$ samples was measured by broth dilution test. The test strains were precultured, and the bacteria was then diluted with sterile physiological saline to prepare a 10^6 CFU/ml bacterial solution. The solution was used as the test stock solution, and the highest concentration was two-fold diluted with a 1% solution, and 10 steps were prepared using Mueller Hinton broth, which is a culture medium for bacteria. $\text{Mo}_{0.55}\text{W}_{0.45}\text{O}_{3-x}$ samples with various amounts of 10–100 mg/ml were added into the tubes. After inoculating one drop of the prepared solution and culturing it at 32°C for a day, the presence or absence of the inoculum growth was visually observed, and the MIC was determined.

2.4.2. Shake-flask method

The sample was placed in a phosphate buffer solution ($\text{pH } 7.0 \pm 0.2$) at a 10 mg/ml ratio, and after inoculation, the culture was shaken at 120 rpm and $35 \pm 1^\circ\text{C}$ for 10 min to 6 h. Similarly, a bacterial solution was inoculated into a phosphate buffer solution, in which no sample was added, which was used as a control. After cultivation, bacterial solutions were collected from test and control samples, diluted with physiological saline, and cultured at $37 \pm 1^\circ\text{C}$ for 24 h using a BHI agar medium to measure the number of bacteria. All experiments were repeated in triplicate the antibacterial reduction and increase rates were calculated as follows:

$$\text{Reduction rate (\%)} = [(A-B)/A] \times 100 \quad (1)$$

A: Numbers of bacteria in the control sample after n h incubation.

B: Numbers of bacteria in the test sample after n h incubation.

The test tube was exposed to light with a compact fluorescent lamp (DULUX L 36 W, white). The samples were placed 1 m away from the lamp for 10 min or 1 h. The control samples were kept at room temperature and under dark conditions. All control tubes without samples are kept under light and dark conditions.

2.4.3. Detection of $\bullet\text{OH}$, ${}^1\text{O}_2$, and O_2^-

The formation of $\bullet\text{OH}$ was measured by using a fluorescence probe

method with coumarin [34]. Coumarin (aqueous solution, 0.1 mM, emission at 392 nm) captures $\bullet\text{OH}$ and produces umbelliferone (455 nm). Photoluminescence spectra were measured by the fluorescence spectrophotometer with the excitation wavelength at 332 nm. The formation of ${}^1\text{O}_2$ was determined by using DPBF (DI water: EtOH = 1:1 (v/v), 0.25 μM) that captures ${}^1\text{O}_2$, resulting in a disappearance of photoluminescence peaks of DPBF [8]. Photoluminescence spectra were measured by the fluorescence spectrophotometer with the excitation wavelength at 400 nm. The procedure of $\bullet\text{OH}$ and ${}^1\text{O}_2$ was the same. 10 mg/ml suspension was prepared dispersing oxide samples in coumarin or DPBF solutions, followed by stirring for 10 min or 1 h under light or dark conditions. After that, clear solution was collected by using syringe filter. The formation of O_2^- was measured by using indirect method [35]. NH_2OH aqueous solution (0.08 mM), FeCl_3 aqueous solution (1 mM), and 1,10-phenanthroline aqueous solution (17.4 mM) were prepared before the test. NH_2OH can be consumed by both O_2^- and FeCl_3 . NH_2OH reduces Fe^{3+} to Fe^{2+} that will react with 1,10-phenanthroline, forming water-soluble metal complexes, we call it Fe-Ph. The procedure is as follows:

- 1) 1 mL of NH_2OH solution was added with 1 mg of oxide sample, followed by stirring for 10 min or 1 h under light or dark conditions.
- 2) Clear solution was acquired by using syringe filter, followed by adding FeCl_3 and 1,10-phenanthroline solutions. The ratio of $\text{NH}_2\text{OH}:\text{FeCl}_3:1,10\text{-phenanthroline}$ should be 1:0.3:0.06 (v:v:v).

2.4.4. 2D PL mapping

2D PL spectra were acquired by using an aqueous suspension (100 ppm) of oxide samples. The excitation wavelength ranges from 350 to 650 nm, and the collected emission wavelength is in the range of 200 to 900 nm.

3. Results and discussion

3.1. Synthesis and characterization of $\text{Mo}_{0.55}\text{W}_{0.45}\text{O}_3$

XRD analysis was performed to confirm the crystallinity of the synthesized NPs. In Fig. 1a, the diffraction angles where $2\theta = 23.16, 24.79, 26.31, 33.61, 34.16$, and 41.51° coincide with the peaks of $\text{W}_{0.4}\text{Mo}_{0.6}\text{O}_3$ samples (JCPDS card no. 76-1280, orthorhombic). The peaks of

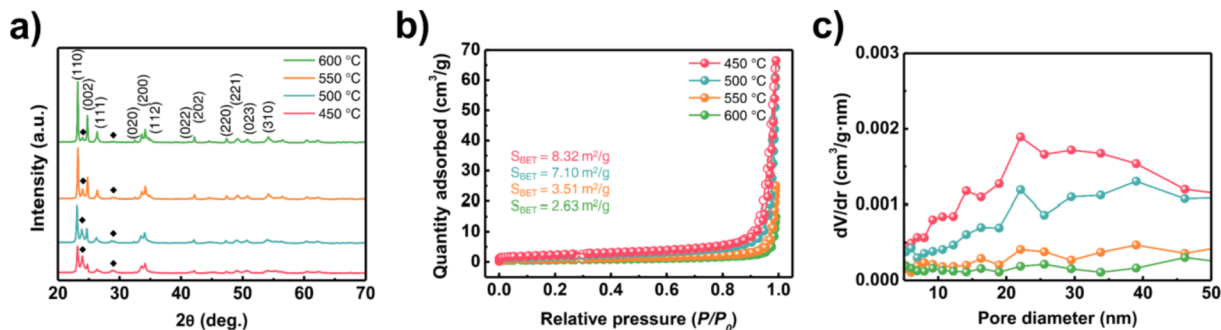


Fig. 1. (a) XRD patterns of Mo_{0.55}W_{0.45}O₃ samples annealed at different temperatures. The black diamonds indicate the peaks of W at the surface, (b) N₂ adsorption–desorption isotherms at 77 K and S_{BET} of and (c) corresponding pore size distribution of Mo_{0.55}W_{0.45}O₃ samples prepared by precipitation at different annealing temperatures.

orthorhombic phases were observed for all samples. The intensity of the (1 1 0) plane peaks was significantly enhanced, indicating that the crystallinity of the (1 1 0) plane in the Mo_{0.55}W_{0.45}O₃ samples intensified as the annealing temperature increased from 450 to 600 °C. The WO₃ peaks in solid diamond were also detected, and their intensities decreased when increasing annealing temperature [36]. This is because W moves from the surface to the interior when increasing temperatures. The average crystallite size for Mo_{0.55}W_{0.45}O₃ samples was estimated using the Scherrer equation: $k\lambda/\beta\cos\theta$, and the values of the lattice parameters obtained by using the Rietveld refinement were displayed in Table S1 [37,38]. At higher annealing temperatures, a large crystallite size is observed due to the increasing mobility of the surface atoms and increasing cluster formation [39,40]. It is observed that the crystallite size increases from 28.69 nm at 450 °C to 53.51 nm at 600 °C. The lattice parameters were determined using $\frac{1}{d^2} = \frac{h^2}{a^2} + \frac{k^2}{b^2} + \frac{l^2}{c^2}$, the standard formula for orthorhombic structures. The lattice parameters $a = 5.331$ Å, $b = 5.519$ Å, and $c = 7.189$ Å of the orthorhombic structure of W_{0.4}Mo_{0.6}O₃ samples were confirmed by adopting the (1 1 0) plane peaks of Mo_{0.55}W_{0.45}O₃ samples.

The S_{BET} of the Mo_{0.55}W_{0.45}O₃ samples annealed at different temperatures was calculated from the N₂ adsorption–desorption isotherms (Fig. 1b), and Barrett–Joyner–Halenda analysis was used to determine the pore size distribution of Mo_{0.55}W_{0.45}O₃ samples (Fig. 1c). According to the IUPAC classification, all these isotherm patterns can be classified as near to type V isotherms, which is a characteristic of stronger adsorbate–adsorbate interactions than adsorbate–adsorbent interactions [41]. The annealing process affects the morphology as well as the surface area (inset in Fig. 1b). S_{BET}s of the Mo_{0.55}W_{0.45}O₃ samples were

8.32, 7.10, 3.51, and 2.63 m²/g for 450, 500, 550, and 600 °C, respectively (Table S2). Total pore volumes for Mo_{0.55}W_{0.45}O₃ sample were 0.09985, 0.09145, 0.03828, and 0.02163 cm³/g for 450, 500, 550, and 600 °C, respectively. The average pore size distribution apparently decreased from 500 to 600 °C, and the total pore volume continued to decrease from 450 to 600 °C, resulting in a marked reduction in the number of pores (Fig. 1c) [42,43].

The morphological features of Mo_{0.55}W_{0.45}O₃ samples annealed at different temperatures were observed using SEM (Fig. 2a–d). The particles were relatively monodispersed with a total diameter of 50–100 nm, and the morphology was mostly spherical when annealed at 450 °C as shown in Fig. 2a. With increasing annealing temperature, the particles began to agglomerate. As shown in Fig. 2b, there is an increase in the size of particles, and no remarkable changes in morphology. Large bulks are, however, observed owing to the agglomeration in Fig. 2c and d. These results suggest that the induced crystallization and transformation could be affected by the annealing temperature. Fig. 2e–h show TEM micrographs of Mo_{0.55}W_{0.45}O₃ samples synthesized at different annealing temperatures. Several different morphologies are observed. For Mo_{0.55}W_{0.45}O₃ sample annealed at 450 °C, irregular spherical particles were observed (Fig. 2e). Similar morphologies were detected in Mo_{0.55}W_{0.45}O₃ sample annealed at 500 °C, although a higher degree of heterogeneity in the shape and size of the nanoparticles was observed (Fig. 2f). Rectangular particles were also formed in small amounts. In Fig. 2g and h, the diameter of the primary particle increased, which was in line with the results of the SEM micrographs. The morphological variation in Mo_{0.55}W_{0.45}O₃ samples coincided well with the S_{BET} results for Mo_{0.55}W_{0.45}O₃ samples. Additionally, a TEM micrograph (Fig. 3a) was taken to explore the microstructure of

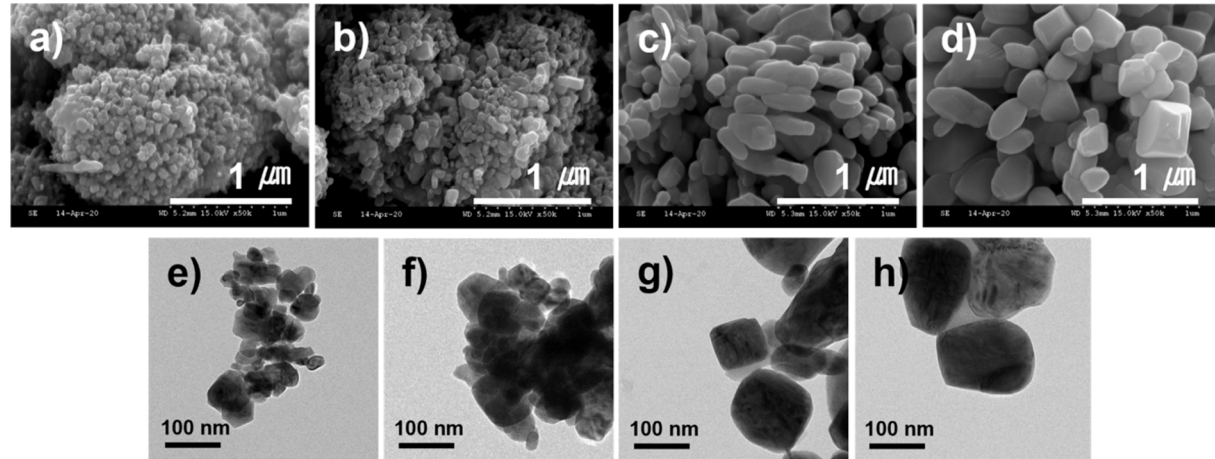


Fig. 2. SEM micrographs of Mo_{0.55}W_{0.45}O₃ samples annealed at different temperatures. (a) 450, (b) 500, (c) 550, and (d) 600 °C. TEM micrographs of Mo_{0.55}W_{0.45}O₃ samples annealed at different temperatures. (e) 450, (f) 500, (g) 550, and (h) 600 °C.

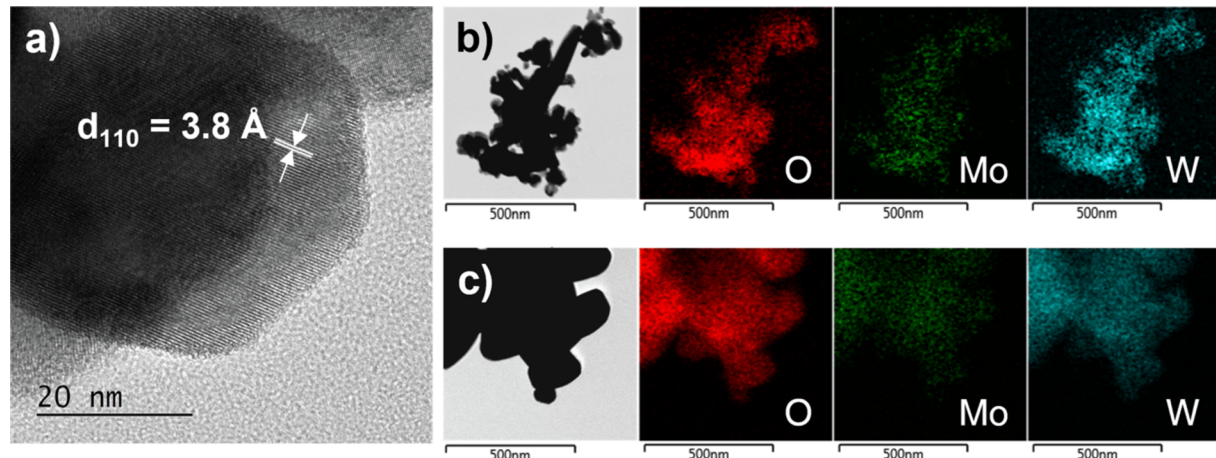


Fig. 3. (a) TEM micrograph of Mo_{0.55}W_{0.45}O₃ samples annealed at 450 °C. EDX mapping images for Mo_{0.55}W_{0.45}O₃ samples annealed at (b) 450 and (c) 600 °C.

Mo_{0.55}W_{0.45}O₃ sample; a fringe spacing of 3.8 Å is observed, corresponding to the (110) plane of Mo_{0.55}W_{0.45}O₃ samples. This result agrees with the XRD analysis. Corresponding EDS mappings of O, Mo, and W from the TEM micrographs were conducted to investigate the distribution of the elements (Fig. 3b and c). The distribution of the three elements was mostly homogeneous, and the distribution of elemental W slightly wider than that of Mo. Although the amount of Mo was greater than W, more W was situated on the surface of Mo_{0.55}W_{0.45}O₃ samples. There is also a subtle difference in the brightness of W in Mo_{0.55}W_{0.45}O₃ samples at 450 and 600 °C; W in Mo_{0.55}W_{0.45}O₃ sample annealed at 600 °C appeared to be brighter than that annealed at 450 °C.

XPS analysis was performed to investigate the surface elemental composition and chemical state of a series of Mo_{0.55}W_{0.45}O₃ samples. The XPS spectra of Mo 3d, W 4f, and O 1 s in Mo_{0.55}W_{0.45}O₃ sample annealed at 450 °C are shown in Fig. 4. There are four primary types of

elements—Mo, W, O, and C—on the composite surface (Fig. 4d). The presence of C is ascribed to adventitious C [44]. The Mo 3d spectrum of Mo_{0.55}W_{0.45}O₃ sample presented in Fig. 4a shows that the Mo 3d spectrum can be well fitted by two 3d doublets in the form of a Gaussian function, corresponding to Mo in two different oxidation states. The major contributor peaks at 233.0 and 236.1 eV are typical values of 3d doublet of Mo⁶⁺ [45]. The minor contributor peaks at 231.8 and 234.8 eV are identified as 3d doublet of Mo⁵⁺ [45]. The atomic ratio of Mo⁵⁺ to Mo⁶⁺ is found to be approximately 0.13. The W 4f spectrum consists of two Gaussian-like 4f doublets, which were identified as W⁶⁺ and W⁵⁺ as shown in Fig. 4b. The major contributor peaks at 35.7 and 37.8 eV are typical values of the 4f doublet of W⁶⁺. The minor contributor peaks at 34.6 and 36.9 eV are typical values 4f doublet of W⁵⁺ [45,46]. Compositional analysis reveals that W⁵⁺ accounts for only approximately 3.8% of total W atoms, and the atomic ratio between Mo, W, and

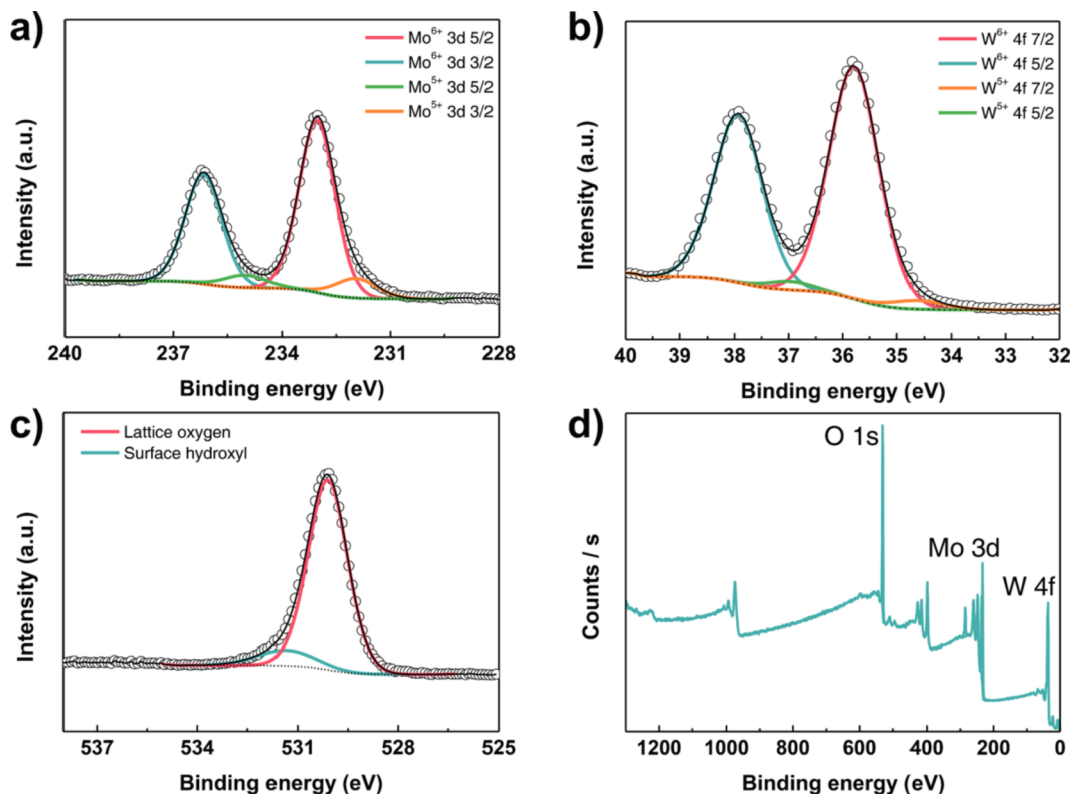


Fig. 4. XPS spectra of Mo_{0.55}W_{0.45}O₃ sample annealed at 450 °C. High-resolution deconvoluted XPS spectra for (a) Mo 3d, (b) W 4f, (c) O 1 s, and (d) XPS survey.

O is approximately 0.53:0.47:2.8. Thus, the surface atomic concentration of $\text{Mo}_{0.55}\text{W}_{0.45}\text{O}_3$ sample annealed at 450 °C has a higher proportion of W than the bulk concentration, which is consistent with the XRD pattern. In addition, the ratio of W to Mo decreases as the annealing temperature increases (Table S3), which is consistent with the reduction in the solid diamond peak in Fig. 1a. Fig. 4c shows the O 1 s spectra of $\text{Mo}_{0.55}\text{W}_{0.45}\text{O}_3$ sample where the spectra of O 1 s are asymmetric and can be deconvoluted into two peaks. The peaks at 530.1 and 531.4 eV can be attributed to lattice oxygen and surface hydroxyl groups bound to oxygen vacancies or defects, respectively [45]. Because the presence of oxygen vacancies is confirmed, we substitute $\text{Mo}_{0.55}\text{W}_{0.45}\text{O}_{3-x}$ for $\text{Mo}_{0.55}\text{W}_{0.45}\text{O}_3$ to clearly express the structural features of $\text{Mo}_{0.55}\text{W}_{0.45}\text{O}_{3-x}$ samples. Oxygen vacancy concentrations and atomic ratios of $\text{Mo}_{0.55}\text{W}_{0.45}\text{O}_{3-x}$ samples acquired from XPS spectra are listed in Table 1. As the annealing temperature increases, the level of oxygen vacancies and the ratios of Mo^{5+} and Mo^{6+} generally decrease, and the ratios of W^{5+} and W^{6+} have similar values.

3.2. Antibacterial activity evaluation

The antibacterial activity of four $\text{Mo}_{0.55}\text{W}_{0.45}\text{O}_{3-x}$ samples was evaluated on two pathogenic bacteria, gram-positive *S. aureus* and gram-negative *E. coli*, by means of the MIC test. MIC values ranged from 12.5 to over 100 mg/ml, and the MIC values of $\text{Mo}_{0.55}\text{W}_{0.45}\text{O}_{3-x}$ samples annealed at 450 and 500 °C to *S. aureus* and *E. coli* were 25 and 12.5 mg/ml (Table S4), respectively. The MIC values of $\text{Mo}_{0.55}\text{W}_{0.45}\text{O}_{3-x}$ annealed at 550 and 600 °C for *S. aureus* and *E. coli* were higher than 25 and 12.5 mg/ml due to their lower S_{BET} . In addition, a quantitative evaluation of antibacterial performance was conducted using the shake flask method, and the results are listed in Table 2. To evaluate the effect of light on the antibacterial activity, we designed light and dark conditions (Scheme 2). First, we consider the tests carried out under light conditions. After 1 h incubation, all $\text{Mo}_{0.55}\text{W}_{0.45}\text{O}_{3-x}$ samples treated at 450, 500, 550, and 600 °C displayed satisfiable antibacterial performance against *S. aureus* with values higher than $97.800 \pm 1.806\%$. For $\text{Mo}_{0.55}\text{W}_{0.45}\text{O}_{3-x}$ samples treated at 450 and 500 °C, antibacterial performance was limited by the detection limit ($>99.996\%$). $\text{Mo}_{0.55}\text{W}_{0.45}\text{O}_{3-x}$ samples treated at 450 and 500 °C exhibited fast and effective antibacterial performance against *E. coli* after 1 h of incubation ($>99.996\%$) whereas the $\text{Mo}_{0.55}\text{W}_{0.45}\text{O}_{3-x}$ samples treated at 550 and 600 °C showed 73.697 ± 2.412 and $44.798 \pm 3.324\%$ activities, respectively. Because the S_{BET} of $\text{Mo}_{0.55}\text{W}_{0.45}\text{O}_{3-x}$ sample treated at 600 °C is approximately one-third of that treated at 450 °C, we also evaluated the performance of $\text{Mo}_{0.55}\text{W}_{0.45}\text{O}_{3-x}$ sample treated at 600 °C with a concentration 3 times higher, and the results were 99.545 ± 1.073 and $92.134 \pm 1.167\%$ for *S. aureus* and *E. coli*, respectively.

In the second stage, we see the antibacterial activity acquired under dark conditions. $\text{Mo}_{0.55}\text{W}_{0.45}\text{O}_{3-x}$ samples treated at 450 and 500 °C maintained good activities of 91.829 ± 1.317 – $99.206 \pm 1.294\%$ with slight deactivation against both *S. aureus* and *E. coli*. The $\text{Mo}_{0.55}\text{W}_{0.45}\text{O}_{3-x}$ samples treated at 550 and 600 °C did not show salient differences under light or dark conditions. It is widely accepted that ROS and H_3O^+ , Mo, and W ions concurrently affect the performance of the oxide-based antibacterial. Therefore, it is highly desirable to identify the influence of each factor on antibacterial performance. Accordingly, even

more strict antibacterial tests were conducted that under light and dark conditions, 10 min incubation for $\text{Mo}_{0.55}\text{W}_{0.45}\text{O}_{3-x}$ samples treated at 450 and 500 °C was carried out. Interestingly, we observed that the antibacterial performances of $\text{Mo}_{0.55}\text{W}_{0.45}\text{O}_{3-x}$ samples treated at 450 and 500 °C significantly reduced to 17.356 ± 4.503 and $20.425 \pm 4.404\%$ under dark conditions, respectively, from 98.846 ± 1.113 and $97.598 \pm 1.193\%$ under light conditions against *S. aureus* and *E. coli*, respectively. It should be noted that the lamp used here is a weak ambient compact fluorescent lamp (white 32 W, near 100 lx and at 1 m away), and the ROS effect seems to be dominant in this system compared to the effect of H_3O^+ and released ions. The ROS effect will be thoroughly discussed in the following section. Petri dish photographs of *S. aureus* and *E. coli* treated with $\text{Mo}_{0.55}\text{W}_{0.45}\text{O}_{3-x}$ samples annealed at 450 and 500 °C under dark and light conditions and the control test under light are displayed in Fig. 5a. There are almost no bacterial colonies for $\text{Mo}_{0.55}\text{W}_{0.45}\text{O}_{3-x}$ samples annealed at 450 and 500 °C under light conditions compared to the numerous bacterial colonies observed in $\text{Mo}_{0.55}\text{W}_{0.45}\text{O}_{3-x}$ samples annealed at 450 and 500 °C under dark conditions and the control experimental conditions. In addition, logarithmic bactericidal kinetic curves of $\text{Mo}_{0.55}\text{W}_{0.45}\text{O}_{3-x}$ samples against *S. aureus* and *E. coli* over time are illustrated in Fig. 5b; within 30 min incubation, the system quickly reached the detection limit.

Antibacterial activities were compared with >20 substances previously reported for action time and residual bacterial colonies (Fig. 6) with the same gram-positive *S. aureus* (ATCC 6538) and gram-negative *E. coli* (ATCC 8739) [47–70]. Ag, Cu, and Zn are the most widely studied substances for antibacterial activity that are usually bonded to graphene to enhance activity [61,63,67,69,70]. Noticeably, $\text{Mo}_{0.55}\text{W}_{0.45}\text{O}_{3-x}$ samples are a high-performance antibacterial substance with respect to low incubation time and residual. In particular, this effect was unrivaled for gram-negative bacteria. The antibacterial activity is even better than that of Cu metal and Ag copolymer beads [57,58], and $\text{Mo}_{0.55}\text{W}_{0.45}\text{O}_{3-x}$ samples is superior to materials such as TiO_2 and $\text{Fe}_3\text{O}_4@\text{Cu-BTC}$ [47,70].

3.3. Detection of ROS generated by MoWO_{3-x}

To assess the effect of each ROS on the antibacterial activity, generation of ROS was detected by using coumarin ($\bullet\text{OH}$ capture agent) [34], DPBF (${}^1\text{O}_2$ scavenger) [8], and Fe-Ph (inverse proportion to O_2^\bullet) [35]. Fig. 7a and d show the amount of umbelliferone (emission at 455 nm) produced by the reaction (inset in Fig. 7d) between coumarin (emission at 392 nm) and $\bullet\text{OH}$. After stirring the suspension made up of coumarin and MoWO_{3-x} samples for 1 h under light conditions, MoWO_{3-x} samples annealed at 450 and 500 °C exhibited intense peak of umbelliferone; whereas those annealed at 550 and 600 °C show moderate peak intensities. Under dark conditions, the peak intensities of umbelliferone for MoWO_{3-x} samples annealed at 450 and 500 °C are moderate, and for MoWO_{3-x} samples annealed at 550 and 600 °C no corresponding peak was observed. Moreover, the double peaks of DPBF disappeared when stirring the suspension of MoWO_{3-x} samples and DPBF solution for 1 h under light conditions (Fig. 7b), and the peaks of DPBF weakened under dark conditions as the annealing temperature goes up (Fig. 7e). These results indicate that all MoWO_{3-x} samples can effectively produce ${}^1\text{O}_2$, according to the reaction (inset in Fig. 7b) at least under light conditions. In addition, from Fig. 7c and f, the characteristic UV-Vis absorption peak of Fe-Ph (the product of the reaction; inset in Fig. 7f) at 511 nm gradually weakened as the annealing temperature goes down under both light (Fig. 7c) and dark (Fig. 7f) conditions, indicating that O_2^\bullet emerged in the system (details see Experimental section). It should be mentioned here that (i) and (ii) are competition reactions (inset in Fig. 7c). Therefore, the peak intensity at 511 nm is inversely proportional to O_2^\bullet generation. Since there is a significant difference in the antibacterial performance of MoWO_{3-x} samples annealed at 450 and 500 °C under dark and light conditions, ROS arising from them were also detected after 10 min stirring with

Table 1

Overview of the estimated oxygen vacancies (δ) of each sample determined from XPS results, where \times represents oxygen stoichiometry.

| Annealing temperature (°C) | Mo^{5+} : Mo^{6+} from XPS | W^{5+} : W^{6+} from XPS | x | $\delta = 3 - x$ |
|----------------------------|----------------------------------------------|--------------------------------------------|------|------------------|
| 450 | 0.13 | 0.04 | 2.80 | 0.20 |
| 500 | 0.12 | 0.04 | 2.82 | 0.18 |
| 550 | 0.15 | 0.05 | 2.95 | 0.05 |
| 600 | 0.20 | 0.05 | 2.88 | 0.12 |

Table 2

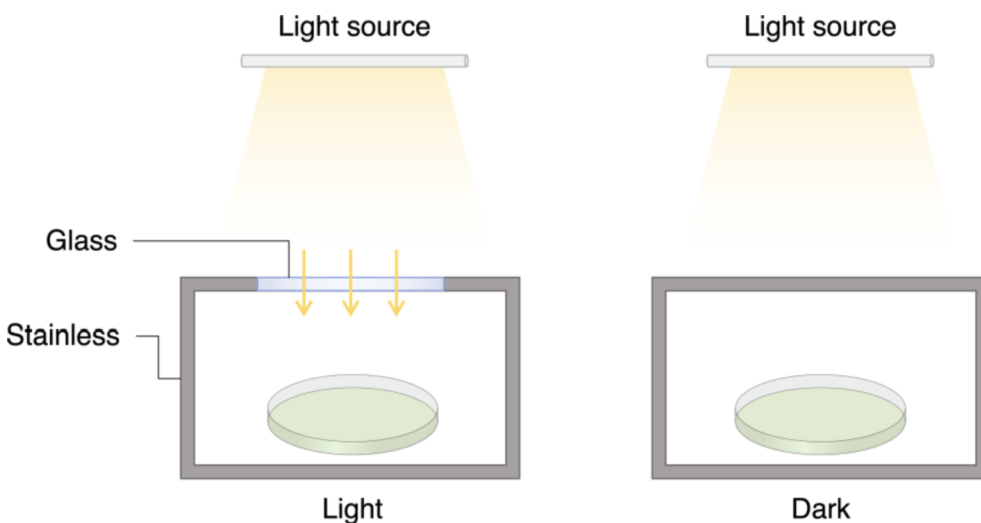
Antibacterial rate of $\text{Mo}_{0.55}\text{W}_{0.45}\text{O}_{3-x}$ samples at different annealing temperatures against *S. aureus* and *E. coli* cultivated under light or dark conditions for different periods. Antibacterial rate is the average of three measurements and the observed standard deviation (SD) is presented.

| $\text{Mo}_{0.55}\text{W}_{0.45}\text{O}_{3-x}$ | Time | gram-positive | Light | Dark | gram-negative | Light | Dark |
|-------------------------------------------------|--------|------------------|------------------------|------------------------|----------------|------------------------|------------------------|
| | | | Antibacterial rate (%) | Antibacterial rate (%) | | Antibacterial rate (%) | Antibacterial rate (%) |
| 450 ^a | 1 h | <i>S. aureus</i> | > 99.996 ^b | 99.206 ± 1.294 | <i>E. coli</i> | > 99.996 ^b | 97.465 ± 1.071 |
| 500 ^a | 1 h | | > 99.996 ^b | 99.179 ± 1.503 | | > 99.996 ^b | 91.829 ± 1.317 |
| 450 ^a | 10 min | | 98.948 ± 1.890 | 17.393 ± 4.454 | | 98.413 ± 1.080 | 20.134 ± 4.002 |
| 500 ^a | 10 min | | 98.846 ± 1.113 | 17.356 ± 4.503 | | 97.598 ± 1.193 | 20.425 ± 4.404 |
| 550 ^a | 1 h | | 98.960 ± 1.052 | 99.185 ± 1.592 | | 73.697 ± 2.412 | 68.092 ± 3.075 |
| 600 ^a | 1 h | | 97.800 ± 1.806 | 97.352 ± 1.098 | | 44.798 ± 3.324 | 44.543 ± 2.764 |
| 600 ^c | 1 h | | 99.545 ± 1.073 | 99.723 ± 1.140 | | 92.134 ± 1.167 | 91.923 ± 1.802 |

^a Shaking culture in a phosphate buffer solution ($\text{pH } 7.0 \pm 0.2$) at a 10 mg/ml ratio at 120 rpm and $35 \pm 1^\circ\text{C}$ for 10 min or 1 h.

^b Evaluation of antibacterial rate was limited by the detection limit ($\geq 10 \text{ CFU/ml}$).

^c Shaking culture in a phosphate buffer solution ($\text{pH } 7.0 \pm 0.2$) at a 30 mg/ml ratio at 120 rpm and $35 \pm 1^\circ\text{C}$ for 1 h.



Scheme 2. Schematic of cultivation conditions for *S. aureus* and *E. coli* in the experiment with $\text{Mo}_{0.55}\text{W}_{0.45}\text{O}_{3-x}$ samples. Left: light from the fluorescent lamp can pass through the topper glass and reach the incubation petri dish; right: the incubation petri dish is isolated from the light.

coumarin, DPBF, and Fe-Ph. The results are displayed in Fig. 8. After the stirring, moderate peaks of umbelliferone were observed under light conditions (Fig. 8a), and there is no discernable umbelliferone peak observed under dark conditions (Fig. 8d). In the case of $^1\text{O}_2$, DPBF was quenched by enough $^1\text{O}_2$ under light conditions (Fig. 8b) whereas the reduction of the double peak of DPBF (Fig. 8e) is similar to that in the case of 1 h stirring (Fig. 7e). Finally, the peak of Fe-Ph at 511 nm after 10 min stirring weakened for all MoWO_{3-x} samples (Fig. 8c and f). In summary, MoWO_{3-x} samples prepared in this work can produce $\bullet\text{OH}$, $^1\text{O}_2$, and $\text{O}_2\bullet^-$ efficiently under light conditions, and the short period of stirring expectedly results in the less amount of generation of ROS. In addition, the same ROS detection was also carried out for the MoWO_{3-x} sample treated at 600°C with 3 times higher concentration of suspensions compared with the other samples mentioned above, and corresponding entries are labeled 3D or 3L (Fig. 7). For the concentrated MoWO_{3-x} sample, the peak intensity of umbelliferone increased, and peak intensities of DPBF and Fe-Ph generally decreased under both light and dark conditions. There are two conspicuous inconsistencies between the poor light irradiation effect of MoWO_{3-x} sample treated at 600°C on antibacterial performance and good ROS generation (entries 600L60 and 600-3L60 in Fig. 7a) and between good light irradiation effect of MoWO_{3-x} sample treated at 450°C on antibacterial performance and moderate ROS generation (Fig. 8a). To scrupulously examine the role of each ROS, we deconvoluted entire Fe-Ph peaks, culled the main spectrum named Peak-1, and displayed the area of Peak-1 in Fig. 9. Detailed data about the deconvolution, the position of, and the area of deconvoluted spectra see Supporting Information (Fig. S1–S4 and Table S5).

3.4. Antibacterial mechanism for MoWO_{3-x}

The remained issue is to elucidate the effect of factors including Mo and W ions, H_3O^+ , and ROS. First, we observed that the molar ratio of W/Mo gradually decreased when the annealing temperature increased from 450 to 600°C via XPS and EDS analyses (Fig. 10a, Table S3, and Fig. S5), which means that as the temperature increases, Mo and W are likely to move to the surface and center of $\text{Mo}_{0.55}\text{W}_{0.45}\text{O}_{3-x}$, respectively. The released Mo and W ions gradually decreased from 87.79 and 14.57 ppm to 29.74 and 5.03 ppm, respectively, when annealing temperature increased (Table 3). In addition, $\text{Mo}_{0.55}\text{W}_{0.45}\text{O}_{3-x}$ treated at 600°C in 3 times higher concentration exhibited a high ion release. The pH values were acquired every 5 min, and the results are shown in Fig. 10b. The pH values dropped rapidly and reached 3.4–3.7. Since it is impossible to distinguish between the effect of Mo and W ions on antibacterial activity and that of H_3O^+ on antibacterial activity, we consider them as a whole. In general, Mo and W ions and H_3O^+ show higher antibacterial activity against *S. aureus* than that against *E. coli*. pH, ion release, and ROS results are combined and displayed in Table 4 in which the values of the antibacterial rate were presented with two decimal places for a better readability. In ROS part in Table 4, the number of asterisks refers to the relative concentration of specific ROS, and slash indicates subtle generation of ROS. It should be noted here that ROS values in Table 4 is the summarization of the data in Figs. 7–9. Light brown-filled part in Table 4 indicate the light sensitive entries. First, we examine the ROS after 1 h stirring. Despite a great amount of $^1\text{O}_2$ generated by $\text{Mo}_{0.55}\text{W}_{0.45}\text{O}_{3-x}$ sample treated at 600°C under light conditions (Fig. 7b), antibacterial

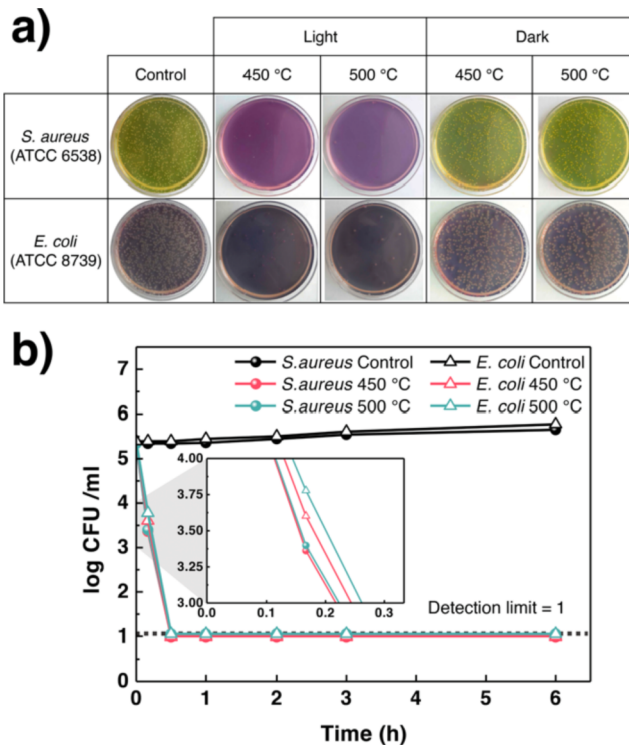


Fig. 5. (a) Petri dish photographs of *S. aureus* and *E. coli* incubated on agar plates with $\text{Mo}_{0.55}\text{W}_{0.45}\text{O}_{3-x}$ samples at different annealing temperatures under light and dark conditions and without $\text{Mo}_{0.55}\text{W}_{0.45}\text{O}_{3-x}$ samples under light conditions as control experiments. (b) Logarithmic bactericidal kinetic curves of $\text{Mo}_{0.55}\text{W}_{0.45}\text{O}_{3-x}$ samples against *S. aureus* and *E. coli* under light conditions.

rates for both *S. aureus* and *E. coli* are independent on these ROS (Table 2 and 4). According to these observations, we can conclude that ${}^1\text{O}_2$ has no discernable effect on killing bacteria as the amount of ${}^1\text{O}_2$ for all $\text{Mo}_{0.55}\text{W}_{0.45}\text{O}_{3-x}$ samples shows similar values under light conditions. In addition, excellent antibacterial performance of $\text{Mo}_{0.55}\text{W}_{0.45}\text{O}_{3-x}$ samples treated at 450 and 500 °C can be attributed to a large amount of $\bullet\text{OH}$ from them (Fig. 7a). Now we consider the results acquired from 10 min stirring (Fig. 8). Despite the moderate peak intensity of umbelliferone, the antibacterial activity of $\text{Mo}_{0.55}\text{W}_{0.45}\text{O}_{3-x}$ samples treated at 450 and 500 °C is good under light conditions (Fig. 8a); the peak of umbelliferone is almost indiscernible under dark conditions (Fig. 8d). Because antibacterial activity was not influenced by ${}^1\text{O}_2$, we do not need to evaluate the variation of the reduction of DPBF peaks (Fig. 8b and e).

Regarding O_2^- , we are going to examine its effect by combining the results of 1 h (Fig. 7c and f) and 10 min (Fig. 8c and f) stirring as a whole. Since the Fe-Ph curves are influenced by both background and the dissolved ions, the deconvolution was carried out as mentioned above (Fig. 9). Compared with the control entry, $\text{Mo}_{0.55}\text{W}_{0.45}\text{O}_3$ sample, the area of Peak-1 of the others diminished regardless of the concentration and test conditions. We divide the reduction into M^{n+} -dominated reduction and O_2^- -dominated reduction. The smaller value of area of Peak-1 is generally consistent with the antibacterial performance except the similarity between L10 (dash orange circle) and entries of $\text{Mo}_{0.55}\text{W}_{0.45}\text{O}_{3-x}$ sample annealed at 600 °C. They have similar values but completely different light sensitivity that the former has ROS-induced antibacterial activity, but the latter has no such activity. Similar phenomena can also be observed in similar moderate peak intensities of $\text{Mo}_{0.55}\text{W}_{0.45}\text{O}_{3-x}$ samples treated at 450 and 500 °C (Fig. 8a) and of $\text{Mo}_{0.55}\text{W}_{0.45}\text{O}_{3-x}$ sample annealed at 600 °C (Fig. 7a). Moreover, the intensity of concentrated $\text{Mo}_{0.55}\text{W}_{0.45}\text{O}_{3-x}$ sample annealed at 600 °C exhibit much higher peak intensity (Fig. 7a). We could tentatively suggest that the only reason for these results should be the separation efficiency or the lifetime of electrons or holes [71,72].

To verify the postulate, we confirmed the band positions of $\text{Mo}_{0.55}\text{W}_{0.45}\text{O}_{3-x}$ samples by using UV-Vis and UPS analyses. UV-Vis absorption spectra of $\text{Mo}_{0.55}\text{W}_{0.45}\text{O}_{3-x}$ samples were shown in Fig. 10c, and the optical E_g of $\text{Mo}_{0.55}\text{W}_{0.45}\text{O}_{3-x}$ samples was determined by adopting the Tauc method. The direct E_g can be calculated from the absorption coefficient (α) and photon energy ($h\nu$) using the following relation:

$$\alpha h\nu = A(h\nu - E_g)^n \quad (2)$$

In this case, n equals 2 (indirect allowed transition dominated). Then, plot $(\alpha h\nu)^{1/2}$ versus $h\nu$ and extrapolate the linear portion to the energy axis to obtain E_g . The E_g values of $\text{Mo}_{0.55}\text{W}_{0.45}\text{O}_{3-x}$ with different annealing temperatures are shown in Fig. 10d and increase from 2.63 to 3.41 eV as temperature increases. As the oxygen vacancies in Table 1 increase, the optical E_g tends to narrow. UPS analysis was conducted to determine the Φ and E_F , and the results are displayed in Fig. 11. The Φ was determined using the UPS spectra of $E_{cut-off}$ for $\text{Mo}_{0.55}\text{W}_{0.45}\text{O}_{3-x}$ samples (Fig. 11a-d). The gap between the E_V and E_F was determined by employing E_{VB} edge for $\text{Mo}_{0.55}\text{W}_{0.45}\text{O}_3$ s (Fig. 11e-h). All the bands acquired from the UPS with E_g are illustrated in Fig. 12. The energy diagram comprises bands and specific values based on our measurements, including E_{vac} , E_C , E_F , E_V , E_g , Φ , and EA. The potential of $\bullet\text{OH}/\text{H}_2\text{O}$, ${}^1\text{O}_2/\text{O}_2$, and O_2/O_2^- couples, the photon energy (2.03–3.05 eV) of the compact fluorescent lamp (E_{lamp}) supplied by the manufacturer is displayed in Fig. 12. Because all $\text{Mo}_{0.55}\text{W}_{0.45}\text{O}_{3-x}$ samples have oxygen vacancies, there must be some E_{trap} . As depicted in Fig. 12, the E_g of

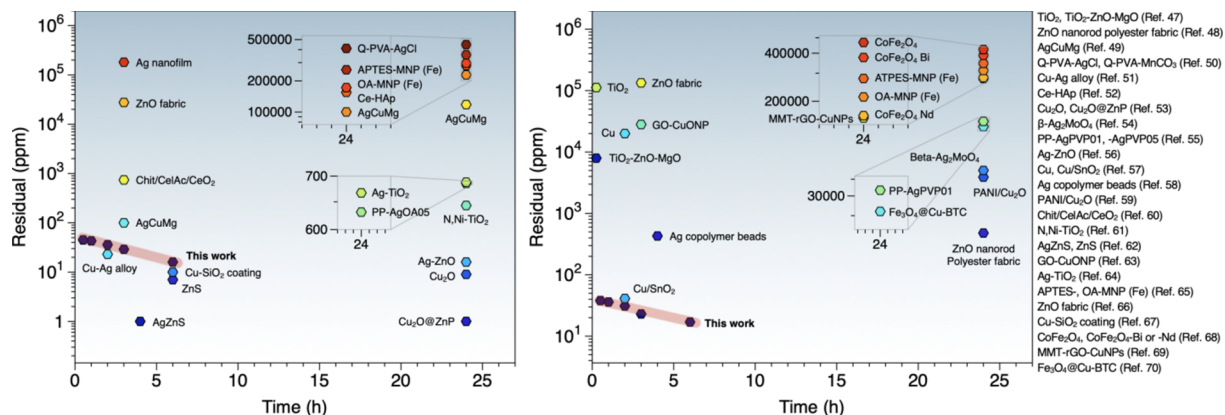


Fig. 6. Active antibacterial materials reported in the literature, including of metal, metal oxide, and polymers. All catalysts shown were tested on the same pathogenic bacteria; (a) *S. aureus* (ATCC 6538) and (b) *E. coli* (ATCC 8739). The cultivating conditions contingent upon the materials. Residual is the ratio of numbers of bacterial colonies in the test sample to that in the control sample in ppm.

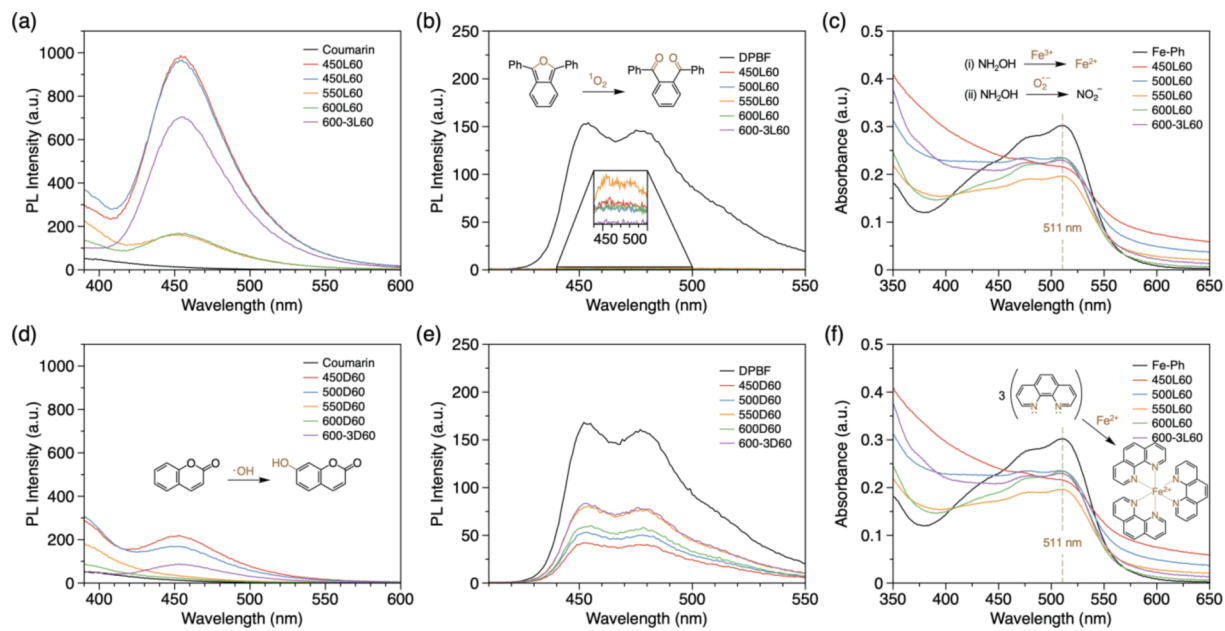


Fig. 7. Detection of ROS generated by $\text{Mo}_{0.55}\text{W}_{0.45}\text{O}_{3-x}$ samples. PL spectra of coumarin solution (0.1 mM) with and without the addition of $\text{Mo}_{0.55}\text{W}_{0.45}\text{O}_{3-x}$ samples (a) under light and (d) dark conditions. PL spectra of DPBF solution (0.25 μM) with and without the addition of $\text{Mo}_{0.55}\text{W}_{0.45}\text{O}_{3-x}$ samples (b) under light and (e) dark conditions. Excitation wavelength was 332 nm. UV-Vis absorption spectra of Fe-Ph solution with and without the addition of $\text{Mo}_{0.55}\text{W}_{0.45}\text{O}_{3-x}$ samples (c) under light and (f) dark conditions. All ROS generations were consummated by stirring the mixture of the specific solution for 60 min. Inset reaction schemes illustrate the possible reactions affected by ROS species.

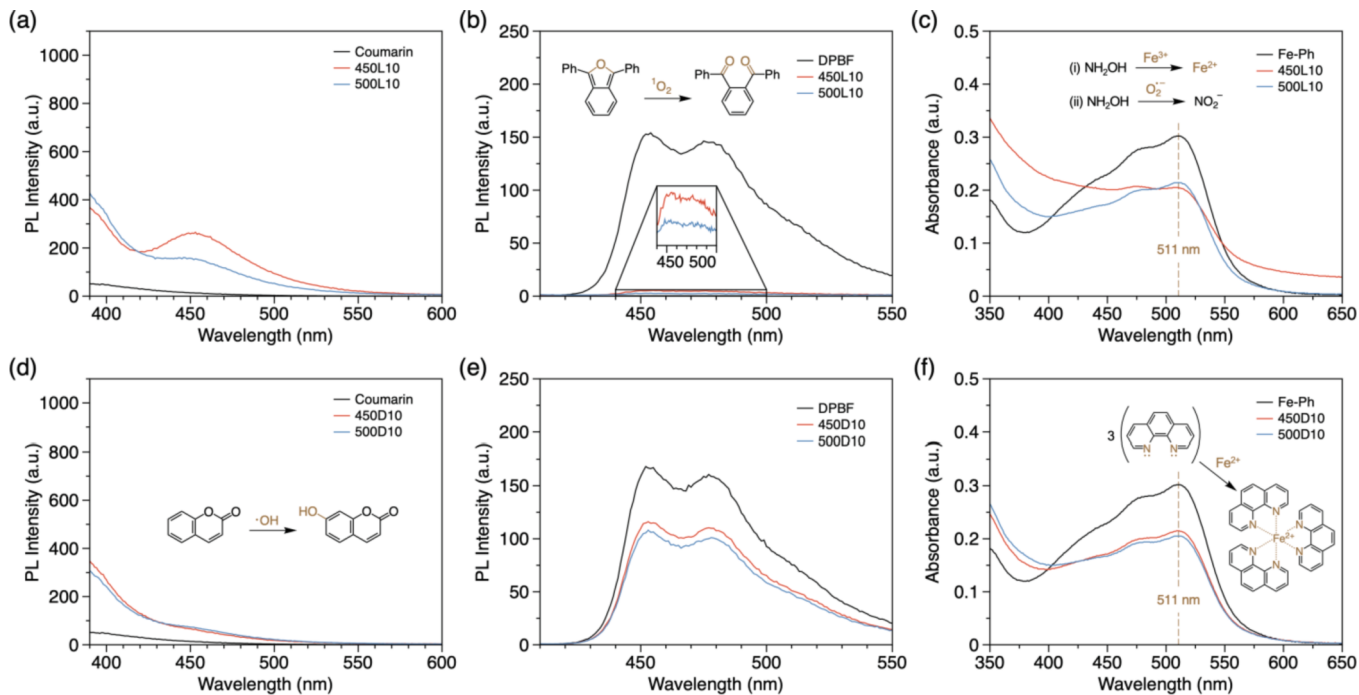


Fig. 8. Detection of ROS generated by $\text{Mo}_{0.55}\text{W}_{0.45}\text{O}_{3-x}$ samples. PL spectra of coumarin solution (0.1 mM) with and without the addition of $\text{Mo}_{0.55}\text{W}_{0.45}\text{O}_{3-x}$ samples (a) under light and (d) dark conditions. PL spectra of DPBF solution (0.25 μM) with and without the addition of $\text{Mo}_{0.55}\text{W}_{0.45}\text{O}_{3-x}$ samples (b) under light and (e) dark conditions. Excitation wavelength was 332 nm. UV-Vis absorption spectra of Fe-Ph solution with and without the addition of $\text{Mo}_{0.55}\text{W}_{0.45}\text{O}_{3-x}$ samples (c) under light and (f) dark conditions. All ROS generations were consummated by stirring the mixture of the specific solution for 10 min. Inset reaction schemes illustrate the possible reactions affected by ROS species.

$\text{Mo}_{0.55}\text{W}_{0.45}\text{O}_{3-x}$ samples are similar or larger than the supplied photon energy from the lamp. Considering the antibacterial performance of $\text{Mo}_{0.55}\text{W}_{0.45}\text{O}_{3-x}$ samples annealed at 450 and 500 °C and the demonstrated LSPR features of oxides containing Mo and W [28–30,33], there should be some E_{trap} between valence and conduction bands of

$\text{Mo}_{0.55}\text{W}_{0.45}\text{O}_{3-x}$ samples, leading to the LSPR effect among $\text{Mo}_{0.55}\text{W}_{0.45}\text{O}_{3-x}$ samples. Unfortunately, we failed to observe the LSPR effect from UV to NIR spectra (Fig. 10c).

To comprehensively assess the emitting property of $\text{Mo}_{0.55}\text{W}_{0.45}\text{O}_{3-x}$ samples, 2D PL spectra were obtained, and the results are shown in

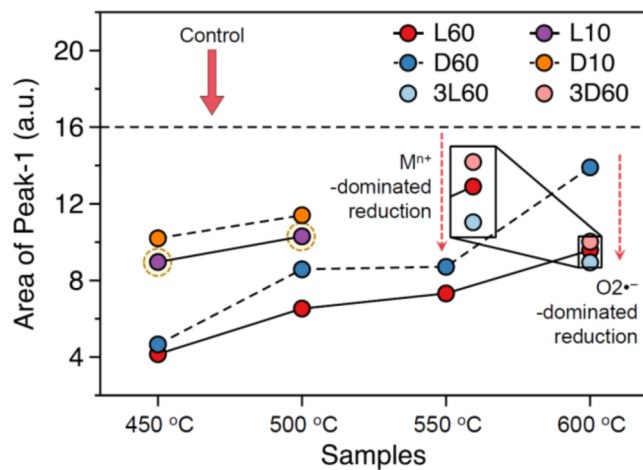


Fig. 9. The area of Peak-1 of the deconvoluted UV-Vis spectra of Fe-Ph solution with $\text{Mo}_{0.55}\text{W}_{0.45}\text{O}_{3-\text{x}}$ samples annealed at different temperatures and $\text{Mo}_{0.55}\text{W}_{0.45}\text{O}_3$ sample as a control entry stirred for a period of 10- or 60-min under light (L) or dark (D) conditions prior to the test. The value, 3, in the legend denotes 3 mg/ml of samples; otherwise, the concentration is 1 mg/ml.

Fig. 13. Apart from the Peak-A, there is an obvious area in the lower right part of each $\text{Mo}_{0.55}\text{W}_{0.45}\text{O}_{3-\text{x}}$ sample embedding representative Peak-B. All $\text{Mo}_{0.55}\text{W}_{0.45}\text{O}_{3-\text{x}}$ samples absorb the photon energy whose wavelength ranges from around 550 to 650 nm and emit the photons with the wavelength of 300 to 400 nm. The emitting intensity goes down when increasing the annealing temperature (Fig. 13f). Apparently, the peak intensity of Peak-B of the control $\text{Mo}_{0.55}\text{W}_{0.45}\text{O}_3$ sample is low because of the lack of oxygen vacancies as well as a paucity of the

consequent E_{trap} (Fig. 13c and f). The 2D PL spectra confirmed the LSPR effect and proved the better performance of $\text{Mo}_{0.55}\text{W}_{0.45}\text{O}_{3-\text{x}}$ samples annealed at 450 and 500 °C than that of $\text{Mo}_{0.55}\text{W}_{0.45}\text{O}_{3-\text{x}}$ samples annealed at 550 and 600 °C with respect to ROS generation. We therefore can conclude that there are two critical features to fulfill the rapid and effectual antibacterial performance of semiconducting oxide-based agents: 1) LSPR effect aiding in extending the scope of the available spectrum and 2) well-formed E_{trap} facilitating the separation of electrons and holes as well as prolonging the lifetime of electrons and holes. By adopting these findings and ideas, we could ascribe the remaining question above, i.e., the two conspicuous inconsistencies discussed in Section 3.3., to the different LSPR effect and varying lifetime of electrons and holes.

4. Conclusions

In this study, $\text{Mo}_{0.55}\text{W}_{0.45}\text{O}_{3-\text{x}}$ samples were successfully synthesized by a coprecipitation of MoO_3 and WO_3 , followed by annealing at 450, 500, 550, and 600 °C to introduce oxygen vacancies as well as E_{trap} . The crystal, surface, and morphological features of $\text{Mo}_{0.55}\text{W}_{0.45}\text{O}_{3-\text{x}}$ samples

Table 3

Concentration of transition metal ions (Mo and W) by ICP-OES in $\text{Mo}_{0.55}\text{W}_{0.45}\text{O}_{3-\text{x}}$ samples at different annealing temperatures.

| Annealing temperature (°C) | Concentration (mg/ml) | ppm Mo | W |
|----------------------------|-----------------------|--------|-------|
| 450 | 10 | 87.49 | 14.57 |
| 500 | 10 | 58.85 | 9.36 |
| 550 | 10 | 39.83 | 6.88 |
| 600 | 10 | 29.74 | 5.03 |
| 600 | 30 | 60.19 | 9.32 |

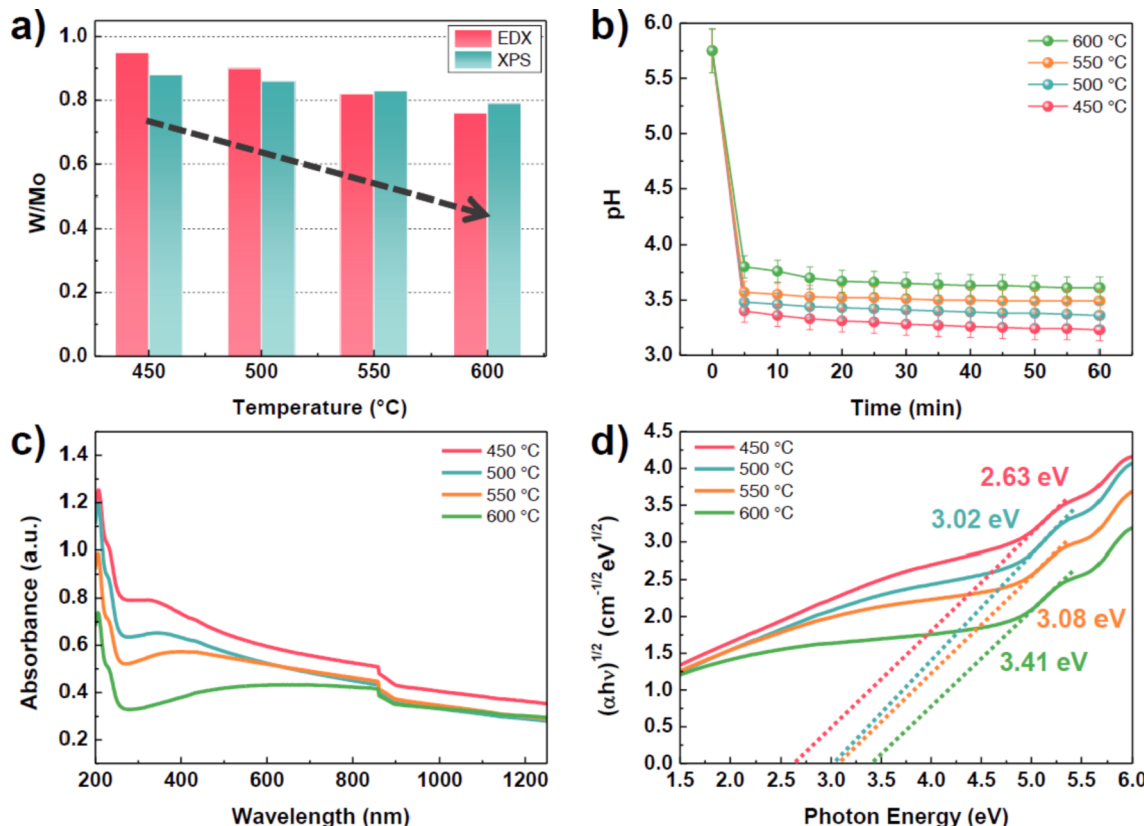


Fig. 10. (a) Results of W/Mo of $\text{Mo}_{0.55}\text{W}_{0.45}\text{O}_{3-\text{x}}$ samples at different annealing temperatures acquired from SEM-EDX and XPS analyses. (b) Changes of pH vs. time which represents the acidity of $\text{Mo}_{0.55}\text{W}_{0.45}\text{O}_{3-\text{x}}$ samples at different annealing temperatures. (c) UV-Vis absorption spectroscopy and (d) Tauc-plots of $\text{Mo}_{0.55}\text{W}_{0.45}\text{O}_{3-\text{x}}$ samples annealed at different temperatures. Error bar for (b) indicates the standard deviation observed for three measurements.

Table 4Assessing the correlation between antibacterial rate and possible effectual factors including of generated ROS, ions, and H_3O^+ .

| Rate | 450 °C | | | | 500 °C | | | | 550 °C | | 600 °C | | 600 °C ^c | |
|------------------------|------------------------------------|--------------------------------------------------------------------------|--------------------------------|--------------------------------|--------------------------|-----------------------------|-----------------------------|---------------------------|----------------------------|----------------------------|-----------------------------|---------------------------|---------------------|--------------------|
| | Dark ^a | Light ^a | Dark ^b | Light ^b | Dark ^a | Light ^a | Dark ^b | Light ^b | Dark ^b | Light ^b | Dark ^b | Light ^b | Dark ^c | Light ^c |
| S. aureus | 17.39 | 98.95 | 99.21 | 100.00 | 17.36 | 98.85 | 99.18 | 100.00 | 99.19 | 98.96 | 97.35 | 97.80 | 99.72 | 99.55 |
| E. coli | 20.13 | 98.41 | 97.47 | 100.00 | 20.43 | 97.60 | 91.83 | 100.00 | 68.09 | 73.70 | 44.54 | 44.80 | 91.92 | 92.13 |
| Factors | R O $\text{O}_2^{\bullet-d}$ | •OH ^d / • O_2 S $\text{O}_2^{\bullet-d}$ | ** *** * **** **** | ** *** * **** **** | / ** * ** ** | ** *** * *** ** | ** *** * *** ** | / ** * *** ** | ** *** * *** * | ** *** * ** ** | */ ** * **** ** | */ ** * ** ** | * | ** |
| M ⁿ⁺ (Mo/W) | 87.5/14.6 | | | | 58.9/9.4 | | | | 39.8/6.9 | | 29.7/5.0 | | 60.2/9.3 | |
| pH | 3.4 | | | | 3.5 | | | | 3.6 | | 3.7 | | 3.5 | |

Shaking culture in a phosphate buffer solution ($\text{pH } 7.0 \pm 0.2$) at a 10 mg/ml ratio at 120 rpm and 35 ± 1 °C for ^a 10 min or ^b 1 h. ^c Shaking culture in a phosphate buffer solution ($\text{pH } 7.0 \pm 0.2$) at a 30 mg/ml ratio at 120 rpm and 35 ± 1 °C for 1 h. ^d The number of asterisks (*) refers to the relative concentration of specific ROS, and slash (/) indicates subtle generation of ROS. The unit of Mⁿ⁺ is ppm.

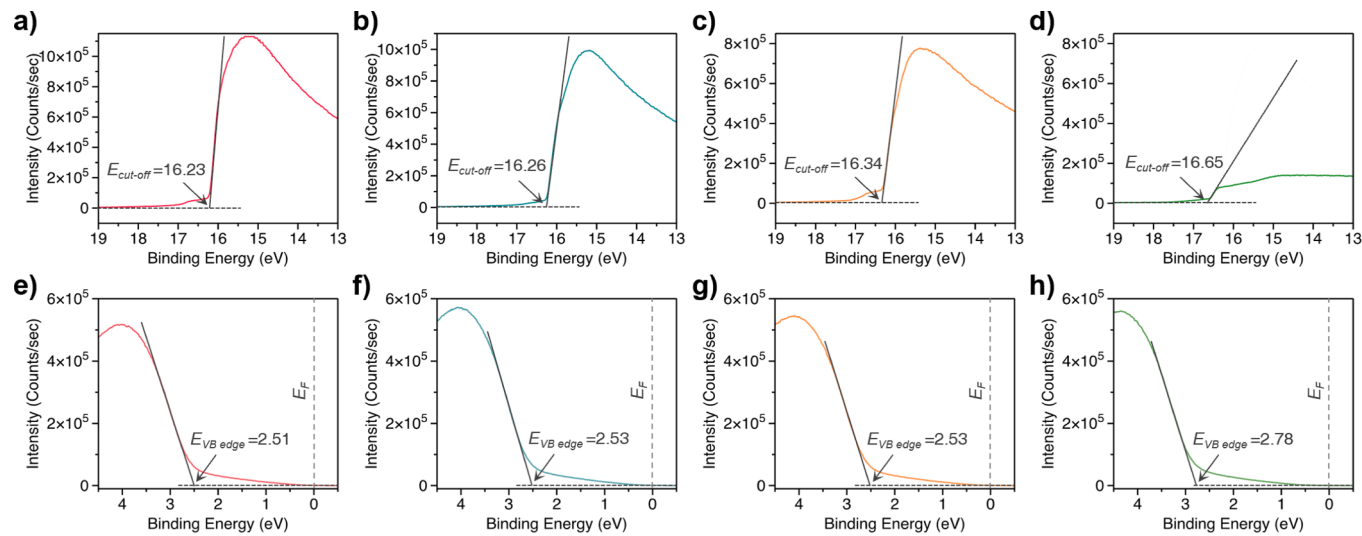
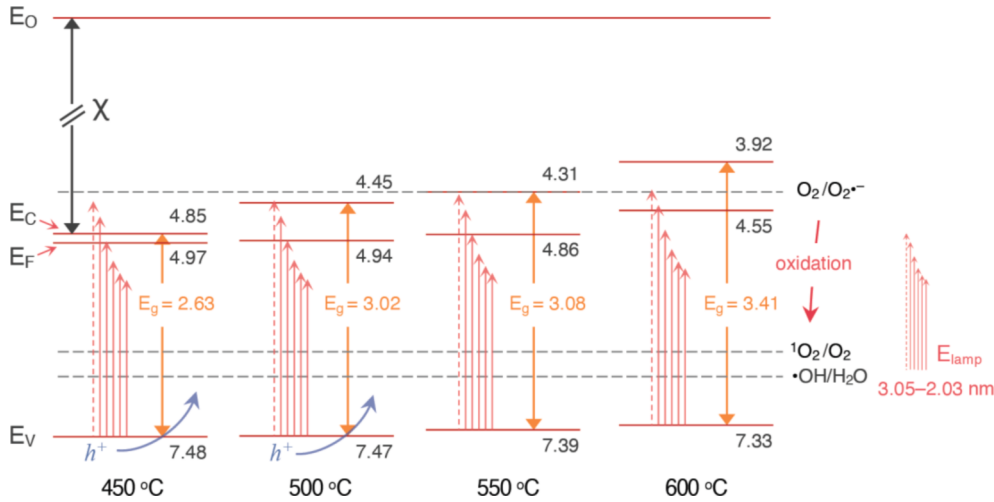


Fig. 11. UPS spectra of secondary electron cut-off region ($E_{\text{cut-off}}$) for $\text{Mo}_{0.55}\text{W}_{0.45}\text{O}_{3-x}$ samples annealed at (a) 450, (b) 500, (c) 550, and (d) 600 °C. UPS spectra of valence band edge region ($E_{\text{VB edge}}$) for $\text{Mo}_{0.55}\text{W}_{0.45}\text{O}_3$ samples annealed at (e) 450, (f) 500, (g) 550, and (h) 600 °C. $E_{\text{VB edge}}$ denotes valence band maximum position with respect with the Fermi level (E_F).



were examined using XRD, BET N₂ adsorption-desorption, SEM, and TEM analyses. Antibacterial activity against gram-positive *S. aureus* (ATCC 6538) and gram-negative *E. coli* (ATCC 8739) was studied under light and dark conditions. All $\text{Mo}_{0.55}\text{W}_{0.45}\text{O}_{3-x}$ samples displayed excellent antibacterial activity after 1 h of incubation (under light:

higher than $97.800 \pm 1.806\%$; under dark: $97.352 \pm 1.098\%$) against *S. aureus*. The $\text{Mo}_{0.55}\text{W}_{0.45}\text{O}_{3-x}$ samples annealed at 450 and 500 °C showed excellent activities: $91.829 \pm 1.317\text{--}99.996\%$ against *E. coli*. Under a stricter condition, i.e., 10 min incubation, $\text{Mo}_{0.55}\text{W}_{0.45}\text{O}_{3-x}$ samples annealed at 450 and 500 °C still exhibited remarkable activities

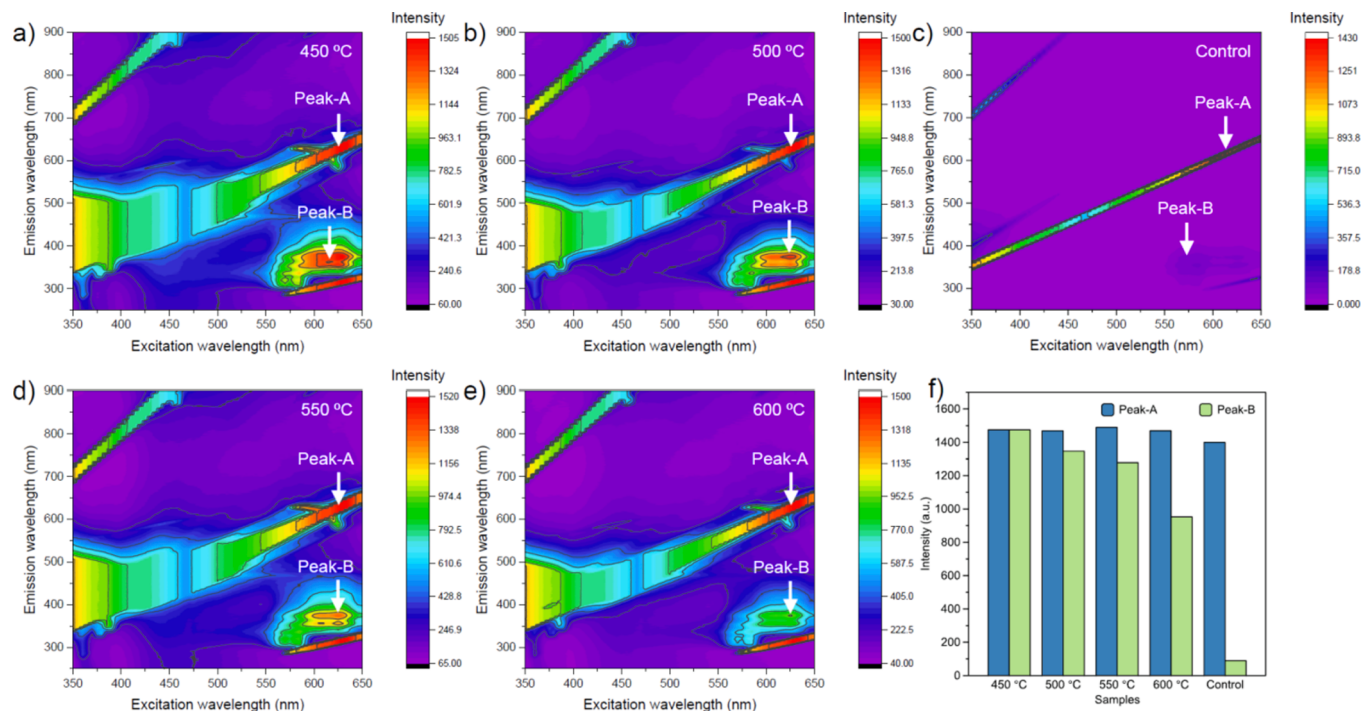


Fig. 13. 2D PL maps in a color scale for $\text{Mo}_{0.55}\text{W}_{0.45}\text{O}_{3-\chi}$ samples annealed at (a) 450, (b) 500, (d) 550, and (e) 600 °C and (c) $\text{Mo}_{0.55}\text{W}_{0.45}\text{O}_3$ sample as a control entry. The excitation ranges from 350 to 650 nm, and the corresponding emission are collected from 200 to 900 nm. Two representative peaks, Peak-A and Peak-B, labeled in each panel arise from the instrument itself and from the samples, respectively. (f) The values of the PL intensity of the samples are displayed.

of 99.206 ± 1.294 and $99.179 \pm 1.503\%$ under light condition. It was confirmed that 1) $^1\text{O}_2$ has no discernable effect on killing both *S. aureus* and *E. coli*, and 2) $\bullet\text{OH}$ and O_2^\bullet kill *S. aureus* and *E. coli* efficiently when combining with LSPR effect and well-formed E_{trap} that are essential features to realize the fast and efficient antibacterial performance, which were proved by using UV–Vis, UPS analyses, and 2D PL spectra. We hope that this work will open new perspectives with respect to antibacterial and semiconducting materials.

CRediT authorship contribution statement

Da Hyeon Shin: Writing – original draft, Investigation. **Sosan Hwang:** Validation, Investigation. **Ye Seo Park:** Visualization. **Jihyun Kim:** Formal analysis. **Seojin Lee:** Formal analysis. **Sanghyun Hong:** Validation, Investigation. **Sang Eun Shim:** Conceptualization, Supervision. **Yingjie Qian:** Supervision, Investigation, Writing – review & editing.

Declaration of Competing Interest

The authors declare that they have no known competing financial interests or personal relationships that could have appeared to influence the work reported in this paper.

Acknowledgments

This work was supported by LG Electronics, Co. Ltd.

Appendix A. Supplementary material

Supplementary data to this article can be found online at <https://doi.org/10.1016/j.apsusc.2022.153496>.

References

- [1] A. Harms, E. Maisonneuve, K. Gerdes, Mechanisms of bacterial persistence during stress and antibiotic exposure, *Science* 354 (2016) aaf4268, <https://doi.org/10.1126/science.aaf4268>.
- [2] World Health Organization, *WHO Report on Surveillance of Antibiotic Consumption: 2016–2018 Early Implementation*, Switzerland, Geneva, 2018.
- [3] AMR Industry Alliance, *AMR Industry Alliance 2020 Progress Report*, Switzerland, Geneva, 2020.
- [4] J. O'Neill, *Tackling Drug-Resistant Infections Globally, Final Report and Recommendations* the Rev. Antimicrobial Resistance (2016).
- [5] U. Kadiyala, N.A. Kotov, J.S. VanEpps, Antibacterial Metal Oxide Nanoparticles: Challenges in Interpreting the Literature, *Curr. Pharm. Des.* 24 (8) (2018) 896–903, <https://doi.org/10.2174/138161282466180219130659>.
- [6] S. Saidin, M.A. Jumat, N.A.A. Mohd Amin, A.S. Saleh Al-Hammadi, Organic and inorganic antibacterial approaches in combating bacterial infection for biomedical application, *Mater. Sci. Eng. C* 118 (2021) 111382, <https://doi.org/10.1016/j.msec.2020.111382>.
- [7] G. Yim, C.Y. Kim, S. Kang, D.-H. Min, K. Kang, H. Jang, Intrinsic Peroxidase-Mimicking Ir Nanoplates for Nanozymatic Anticancer and Antibacterial Treatment, *ACS Appl. Mater. Interfaces* 12 (37) (2020) 41062–41070, <https://doi.org/10.1021/acsami.0c1098110.1021.acsami.0c10981.s001>.
- [8] Y. Zhong, T. Wang, Z. Lao, M. Lu, S. Liang, X. Cui, Q.-L. Li, S. Zhao, Au-Au/IrO₂@Cu(PABA) Reactor with Tandem Enzyme-Mimicking Catalytic Activity for Organic Dye Degradation and Antibacterial Application, *ACS Appl. Mater. Interfaces* 13 (18) (2021) 21680–21692, <https://doi.org/10.1021/acsami.1c00126.1021.acsami.1c00126.s001>.
- [9] A. Panacek, L. Kvitek, M. Smekalova, R. Vecerova, M. Kolar, M. Roderova, F. Dycka, M. Sebele, R. Prucek, O. Tomanec, R. Zboril, Bacterial Resistance to Silver Nanoparticles and How to Overcome It, *Nat. Nanotechnol.* 13 (1) (2018) 65–71, <https://doi.org/10.1038/s41565-017-0013-y>.
- [10] B. Abebe, E.A. Zereffa, A. Tadesse, H.C.A. Murthy, A Review on Enhancing the Antibacterial Activity of ZnO: Mechanisms and Microscopic Investigation, *Nanoscale Res. Lett.* 15 (2020) 190, <https://doi.org/10.1186/s11671-020-03418-6>.
- [11] S.V. Gudkov, D.E. Burmistrov, D.A. Serov, M.B. Rebezov, A.A. Semenova, A. B. Lisitsyn, Do Iron Oxide Nanoparticles Have Significant Antibacterial Properties? *Antibiotics* 10 (7) (2021) 884, <https://doi.org/10.3390/antibiotics10070884>.
- [12] V. Kumaravel, K.M. Nair, S. Mathew, J. Bartlett, J.E. Kennedy, H.G. Manning, B. J. Whelan, N.S. Leyland, S.C. Pillai, Antimicrobial TiO₂ Nanocomposite Coatings for Surfaces, Dental and Orthopaedic Implants, *Chem. Eng. J.* 416 (2021) 129071, <https://doi.org/10.1016/j.cej.2021.129071>.
- [13] S. Pang, Y. He, R. Zhong, Z. Guo, P. He, C. Zhou, B. Xue, X. Wen, H. Li, Multifunctional ZnO/TiO₂ Nanoarray Composite Coating with Antibacterial Activity, Cytocompatibility and Piezoelectricity, *Ceram. Int.* 45 (2019) 12663–12671, <https://doi.org/10.1016/j.ceramint.2019.03.076>.

- [14] T. Munawar, S. Yasmeen, M. Hasan, K. Mahmood, A. Hussain, A. Ali, M.I. Arshad, F. Iqbal, Novel Tri-Phase Heterostructured ZnO-Yb₂O₃-Pr₂O₃ Nanocomposite, Structural, Optical, Photocatalytic and Antibacterial Studies, Ceram. Int. 46 (8) (2020) 11101–11114, <https://doi.org/10.1016/j.ceramint.2020.01.130>.
- [15] Y. Yan, C. Soraru, V. Keller, N. Keller, L. Ploux, Antibacterial and Biofilm-Preventive Photocatalytic Activity and Mechanisms on P/F-Modified TiO₂ Coatings, ACS Appl. Bio Mater. 3 (9) (2020) 5687–5698, <https://doi.org/10.1021/acsabm.0c0046710.1021/acsabm.0c00467.s001>.
- [16] Y. Ji, Z. Han, H. Ding, X. Xu, D. Wang, Y. Zhu, F. An, S. Tang, H. Zhang, J. Deng, Q. Zhou, Enhanced Eradication of Bacterial/Fungi Biofilms by Glucose Oxidase-Modified Magnetic Nanoparticles as a Potential Treatment for Persistent Endodontic Infections, ACS Appl. Mater. Interfaces 13 (15) (2021) 17289–17299, <https://doi.org/10.1021/acsami.1c0174810.1021/acsami.1c01748.s001>.
- [17] S. Jordan, M.I. Hutchings, T. Mascher, Cell Envelope Stress Response in Gram-positive Bacteria, FEMS Microbiol. Rev. 32 (1) (2008) 107–146, <https://doi.org/10.1111/j.1574-6976.2007.00091.x>.
- [18] Y.L. Tseng, K.D. Ambrose, S. Zughaiher, X. Zhou, Y.K. Miller, W.M. Shafer, D. S. Stephens, Cationic Antimicrobial Peptide Resistance in Neisseria Meningitidis, J. Bacteriol. 187 (15) (2005) 5387–5396, <https://doi.org/10.1128/JB.187.15.5387-5396.2005>.
- [19] O. Kolaj-Robin, D. Russell, K.A. Hayes, J.T. Pembroke, T. Soulimane, Cation Diffusion Facilitator Family: Structure and Function, FEBS Lett. 589 (2015) 1283–1295, <https://doi.org/10.1016/j.febslet.2015.04.007>.
- [20] J.M. Arguello, T. Padilla-Benavides, J.M. Collins, Transport Mechanism and Cellular Functions of Bacterial Cu (I)-ATPases, Met. Cells 155 (2016).
- [21] J. van der Heijden, S.L. Vogt, L.A. Reynolds, J. Pena-Diaz, A. Tupin, L. Aussel, B. B. Finlay, Exploring the Redox Balance inside Gram-negative Bacteria with Redox-Sensitive GFP, Free Radic. Biol. Med. 91 (2016) 34–44, <https://doi.org/10.1016/j.freeradbiomed.2015.11.029>.
- [22] V.V. Loi, M. Rossius, H. Antelmann, Redox Regulation by Reversible Protein S-thiolation in Bacteria, Front. Microbiol. 6 (2015) 187, <https://doi.org/10.3389/fmicb.2015.00187>.
- [23] T. Rochat, P. Nicolas, O. Delumeau, A. Rabatinova, J. Korelusova, A. Leduc, P. Bessieres, E. Dervyn, L. Krasny, P. Noirot, Genome-wide Identification of Genes Directly Regulated by the Pleiotropic Transcription Factor Spx in *Bacillus subtilis*, Nucleic Acids Res. 40 (2012) 9571–9583, <https://doi.org/10.1093/nar/gks755>.
- [24] A. Tkachenko, Stress Responses of Bacterial Cells as Mechanism of Development of Antibiotic Tolerance, Appl. Biochem. Microbiol. 54 (2018) 108–127, <https://doi.org/10.1134/S0003683818020114>.
- [25] Y. Li, W. Zhang, J. Niu, Y. Chen, Mechanism of Photogenerated Reactive Oxygen Species and Correlation with the Antibacterial Properties of Engineered Metal-Oxide Nanoparticles, ACS Nano 6 (6) (2012) 5164–5173, <https://doi.org/10.1021/nn300934k>.
- [26] F. Yang, L. Zhou, X. Dong, W. Zhang, S. Gao, X. Wang, L. Li, C. Yu, Q. Wang, A. Yuan, J. Chen, Visible Light-Responsive Nanofibrous α -Fe₂O₃ Integrated FeO_x Clusters Tempted Siliceous Microsheet for Rapid Catalytic Phenol Removal and Enhanced Antibacterial Activity, ACS Appl. Mater. Interfaces 13 (2021) 19803–19815, <https://doi.org/10.1021/acsami.1c04123>.
- [27] J. Yang, C. Wang, X. Liu, Y.i. Yin, Y.-H. Ma, Y. Gao, Y. Wang, Z. Lu, Y. Song, Gallium-Carbonilic Framework Coated Defect-Rich Hollow TiO₂ as a Photocatalyzed Oxidative Stress Amplifier against Complex Infections, Adv. Funct. Mater. 30 (43) (2020) 2004861, <https://doi.org/10.1002/adfm.202004861>.
- [28] M.A. Hosseini, M. Ranjbar, M. Sajadi, Au-MoO_x Nanoparticles for LSPR Hydrogen Detection Prepared by a Facile Anodizing Method, Phys. Lett. A 384 (3) (2020), 126079, <https://doi.org/10.1016/j.physleta.2019.126079>.
- [29] W. Huang, J. Wang, L. Bian, C. Zhao, D. Liu, C. Guo, B. Yang, W. Cao, Oxygen Vacancy Induces Self-Doping Effect and Metalloid LSPR in Non-Stoichiometric Tungsten Suboxide Synergistically Contributing to the Enhanced Photoelectrocatalytic Performance of WO_{3-x}/TiO_{2-x} Heterojunction, Phys. Chem. Chem. Phys. 20 (2018) 17268–17278, <https://doi.org/10.1039/C8CP02044B>.
- [30] Y. Guo, B. Chang, T. Wen, S. Zhang, M. Zeng, N. Hu, Y. Su, Z. Yang, B. Yang, A Z-scheme Photocatalyst for Enhanced Photocatalytic H₂ Evolution, Constructed by Growth of 2D Plasmonic MoO_{3-x} Nanoplates onto 2D g-C₃N₄ Nanosheets, J. Colloid Interface Sci. 567 (2020) 213–223, <https://doi.org/10.1016/j.jcis.2020.01.090>.
- [31] Q.i. Liu, F. Wang, H. Lin, Y. Xie, N.a. Tong, J. Lin, X. Zhang, Z. Zhang, X. Wang, Surface Oxygen Vacancy and Defect Engineering of WO₃ for Improved Visible Light Photocatalytic Performance, Catal. Sci. Technol. 8 (17) (2018) 4399–4406, <https://doi.org/10.1039/C8CY00994E>.
- [32] H.-S. Kim, J.B. Cook, H. Lin, J. Ko, S. Tolbert, V. Ozolins, B. Dunn, Oxygen Vacancies Enhance Pseudocapacitive Charge Storage Properties of MoO_{3-x}, Nat. Mater. 16 (4) (2017) 454–460, <https://doi.org/10.1038/nmat4810>.
- [33] Y. Liu, X. Dong, Q. Yuan, J. Liang, Y. Zhou, X. Qu, B. Dong, In-Situ Synthesis of WO_{3-x}/MoO_{3-x} Heterojunction with Abundant Oxygen Vacancies for Efficient Photocatalytic Reduction of CO₂, Colloids Surf. A 621 (2021) 126582, <https://doi.org/10.1016/j.colsurfa.2021.126582>.
- [34] J. Zhang, Y. Nosaka, Quantitative Detection of OH Radicals for Investigating the Reaction Mechanism of Various Visible-Light TiO₂ Photocatalysts in Aqueous Suspension, J. Phys. Chem. C 117 (3) (2013) 1383–1391, <https://doi.org/10.1021/jp3105166>.
- [35] J. Yang, Y. Cao, N. Zhang, Spectrophotometric Method for Superoxide Anion Radical Detection in a Visible Light (400–780 nm) System, Spectrochim. Acta A Mol. Biomol. Spectrosc. 239 (2020), 118556, <https://doi.org/10.1016/j.saa.2020.118556>.
- [36] W.R.K. Thalgampitiya, T.K. Kapuge, J. He, D. Rathnayake, P. Kerns, S.L. Suib, Mesoporous Molybdenum-Tungsten Mixed Metal Oxide: A Solid Acid Catalyst for Green, Highly Efficient sp³-sp² C-C Coupling Reactions, ACS Appl. Mater. Interfaces 12 (5) (2020) 5990–5998, <https://doi.org/10.1021/acsami.9b2163310.1021/acsami.9b21633.s001>.
- [37] E.H. Kisi, C.J. Howard, R.J. Hill, Crystal Structure of Orthorhombic Zirconia in Partially Stabilized Zirconia, J. Am. Ceram. Soc. 72 (9) (1989) 1757–1760, <https://doi.org/10.1111/j.1151-2916.1989.tb06322.x>.
- [38] L.B. McCusker, R.B. Von Dreele, D.E. Cox, D. Louër, P. Scardi, Rietveld Refinement Guidelines, J. Appl. Crystallogr. 32 (1) (1999) 36–50, <https://doi.org/10.1107/S0021889898009856>.
- [39] H. Kleemann, C. Schuenemann, A.A. Zakhidov, M. Riede, B. Lüssem, K. Leo, Structural Phase Transition in Pentacene Caused by Molecular Doping and its Effect on Charge Carrier Mobility, Org. Electron. 13 (1) (2012) 58–65, <https://doi.org/10.1016/j.orgel.2011.09.027>.
- [40] S. Hegde, A. Kunjomana, P. Murahari, B. Prasad, K. Ramesh, Vacuum Annealed Tin Sulfide (SnS) Thin Films for Solar Cell Applications, Surf. Interfaces 10 (2018) 78–84, <https://doi.org/10.1016/j.surfin.2017.12.003>.
- [41] M.D. Donohue, G. Aranovich, A New Classification of Isotherms for Gibbs Adsorption of Gases on Solids, Fluid Phase Equilib. 158 (1999) 557–563, [https://doi.org/10.1016/S0378-3812\(99\)00074-6](https://doi.org/10.1016/S0378-3812(99)00074-6).
- [42] Y. Ren, P. King, Y. Yang, T. Xiao, C. Chu, S. Gulizia, A. Murphy, Characterization of Heat Treatment-Induced Pore Structure Changes in Cold-Sprayed Titanium, Mater. Charact. 132 (2017) 69–75, <https://doi.org/10.1016/j.matchar.2017.08.006>.
- [43] J. Bahadur, D. Sen, S. Mazumder, S. Ramanathan, Effect of Heat Treatment on Pore Structure in Nano-Crystalline NiO: A Small Angle Neutron Scattering Study, J. Solid State Chem. 181 (5) (2008) 1227–1235, <https://doi.org/10.1016/j.jssc.2008.01.050>.
- [44] G. Greczynski, L. Hultman, X-ray Photoelectron spectroscopy: towards reliable binding energy referencing, Prog. Mater. Sci. 107 (2020) 100591, <https://doi.org/10.1016/j.jpmatsci.2019.100591>.
- [45] X. Tang, J. Liu, K.e. Zhan, H. Sun, B. Zhao, Y.a. Yan, Molybdenum-tungsten Oxide Nanowires Rich in Oxygen Vacancies as An Advanced Electrocatalyst for Hydrogen Evolution, Chem. - Asian J. 15 (19) (2020) 2984–2991, <https://doi.org/10.1002/asia.202000822>.
- [46] S. Corby, L. Francàs, A. Kafizas, J.R. Durrant, Determining the Role of Oxygen Vacancies in the Photoelectrocatalytic Performance of WO₃ for Water Oxidation, Chem. Sci. 11 (11) (2020) 2907–2914, <https://doi.org/10.1039/C9SC06325K>.
- [47] L.M. Anaya-Esparza, N. Gonzalez-Silva, E.M. Yahia, O.A. Gonzalez-Vargas, E. Montalvo-Gonzalez, A. Perez-Larios, Effect of TiO₂-ZnO-MgO Mixed Oxide on Microbial Growth and Toxicity against Artemia salina, Nanomaterials 9 (7) (2019) 992, <https://doi.org/10.3390/nano9070992>.
- [48] M. Ashraf, F. Dumont, C. Campagne, P. Champagne, A. Perwuelz, A. Leriche, N.-E. Chihib, Development of Antibacterial PF by Growth of ZnO Nanorods, J. Eng. Fibers Fabr. 9 (2014) 15–22, <https://doi.org/10.1177/1558925014090090103>.
- [49] G. Benetti, E. Cavalieri, R. Brescia, S. Salassi, R. Ferrando, A. Vantomme, L. Pallecchi, S. Pollini, S. Boncompagni, B. Fortuni, M.J. Van Bael, F. Banfi, L. Gavioli, Tailored Ag-Cu-Mg Multielemental Nanoparticles for Wide-Spectrum Antibacterial Coating, Nanoscale 11 (4) (2019) 1626–1635, <https://doi.org/10.1039/C8NR08375D>.
- [50] C. Carolina, E. Flórez López, V. John, G. Jhon, Á.-T. Yenny, Antimicrobial Surfaces of Metal Halides Immobilized on Polymeric Materials, J. Phys.: Conf. Ser. 1541 (1) (2020) 012004, <https://doi.org/10.1088/1742-6596/1541/1/012004>.
- [51] N. Ciacotich, K.N. Kragh, M. Lichtenberg, J.E. Tesdorpf, T. Bjarnsholt, L. Gram, In Situ Monitoring of the Antibacterial Activity of a Copper-Silver Alloy Using Confocal Laser Scanning Microscopy and pH Microsensors, Glob. Chall. 3 (11) (2019) 1900044, <https://doi.org/10.1002/gch2.201900044>.
- [52] C. Ciobanu, C. Popa, D. Predoi, Cerium Doped Hydroxyapatite Nanoparticles Synthesized by Coprecipitation Method, J. Serb. Chem. Soc. 81 (4) (2016) 433–446, <https://doi.org/10.2298/JSC150824007C>.
- [53] I. Codipa, D.M. Caplan, E.-C. Drăgușescu, B.-A. Lixandru, I.L. Coldea, C.C. Dragomirescu, C. Surdu-Bob, M. Bădulescu, Antimicrobial Activity of Copper and Silver Nanofilms on Nosocomial Bacterial Species, Roum. Arch. Microbiol. Immunol. 69 (2010) 204–212.
- [54] C.C. De Foggi, R.C. De Oliveira, M. Assis, M.T. Fabbro, V.R. Mastelaro, C. E. Vergani, L. Gracia, J. Andrés, E. Longo, A.L. Machado, Unveiling the role of β -Ag₂MoO₄ microcrystals to the improvement of antibacterial activity, Mater. Sci. Eng. C 111 (2020) 110765, <https://doi.org/10.1016/j.msec.2020.110765>.
- [55] E. Fages, J. Pascual, O. Fenollar, D. García-Sanquer, R. Balart, Study of Antibacterial Properties of Polypropylene Filled with Surfactant-Coated Silver Nanoparticles Polym., Eng. Sci. 51 (4) (2011) 804–811, <https://doi.org/10.1002/pen.21889>.
- [56] F. Fontecha-Umana, A.G. Rios-Castillo, C. Ripolles-Avila, J.J. Rodriguez-Jerez, Antimicrobial Activity and Prevention of Bacterial Biofilm Formation of Silver and Zinc Oxide Nanoparticle-Containing Polyester Surfaces at Various Concentrations for Use, Foods 9 (4) (2020) 442, <https://doi.org/10.3390/foods9040442>.
- [57] T. Fukumura, E. Sambandan, H. Yamashita, Preparation, Characterizations, and Antibacterial Properties of Cu/SnO₂ Nanocomposite Bilayer Coatings, J. Coat. Technol. Res. 15 (2) (2018) 437–443, <https://doi.org/10.1007/s11998-017-0017-4>.
- [58] D. Gangadharan, K. Harshvardan, G. Gnanasekar, D. Dixit, K.M. Popat, P.S. Anand, Polymeric Microspheres containing Silver Nanoparticles as a Bactericidal Agent for Water Disinfection, Water Res. 44 (18) (2010) 5481–5487, <https://doi.org/10.1016/j.watres.2010.06.057>.
- [59] K. Gopalakrishnan, C. Ramesh, V. Ragunathan, M. Thamilselvan, Antibacterial Activity of Cu₂O Nanoparticles on *E. coli* Synthesized from Tridax procumbens Leaf Extract and Surface Coating with Polyaniiline, Digest J. Nanomat. Biostruct. 7 (2012) 833–839.

- [60] Z. Kalaycioğlu, N. Kahya, V. Adımcılar, H. Kaygusuz, E. Torlak, G. Akin-Evingür, F. B. Erim, Antibacterial Nano Cerium Oxide/Chitosan/Cellulose Acetate Composite Films as Potential Wound Dressing, *Eur. Polym. J.* 133 (2020) 109777, <https://doi.org/10.1016/j.eurpolymj.2020.109777>.
- [61] B.-G. Park, C.-H. Lee, K.-H. Chung, Visible Light Photocatalytic Activity of Thin Film Coated on Polycarbonate Surface with N- and Ni-Codoped TiO₂ Photocatalyst, *Catalysts* 10 (11) (2020) 1237, <https://doi.org/10.3390/catal10111237>.
- [62] S. Pourmoslemi, F. Seif, R. Mahjub, Enhanced Antibacterial Activity of Ag-doped ZnS Nanoparticles synthesised by a Microwave-Assisted Polyol Method, *Mater. Res. Innov.* 25 (7) (2021) 399–403, <https://doi.org/10.1080/14328917.2020.1831151>.
- [63] P. Rajapaksha, S. Cheeseman, S. Hombsch, B.J. Murdoch, S. Gangadoo, E. W. Blanch, Y. Truong, D. Cozzolino, C.F. McConville, R.J. Crawford, V.K. Truong, A. Elbourne, J. Chapman, Antibacterial Properties of Graphene Oxide-Copper Oxide Nanoparticle Nanocomposites, *ACS Appl. Bio Mater.* 2 (12) (2019) 5687–5696, <https://doi.org/10.1021/acsabm.9b0075410.1021/acsabm.9b00754.s001>.
- [64] S.-Y. Ryu, J.W. Chung, S.-Y. Kwak, Dependence of Photocatalytic and Antimicrobial Activity of Electrospun Polymeric Nanofiber Composites on the Positioning of Ag-TiO₂ Nanoparticles, *Compos. Sci. Technol.* 117 (2015) 9–17, <https://doi.org/10.1016/j.compscitech.2015.05.014>.
- [65] R.I. Shebl, F. Farouk, H.-M.-E.-S. Azzazy, Effect of Surface Charge and Hydrophobicity Modulation on the Antibacterial and Antibiofilm Potential of Magnetic Iron Nanoparticles, *J. Nanomater.* 2017 (2017) 1–15, <https://doi.org/10.1155/2017/3528295>.
- [66] G. Singh, E.M. Joyce, J. Beddow, T.J. Mason, Evaluation of Antibacterial Activity of ZnO Nanoparticles Coated Sonochemically onto Textile Fabrics, *J. Microbiol. Biotechnol. Food Sci.* 2 (2020) 106–120.
- [67] S. Varghese, S.O. Elfakhri, D.W. Sheel, P. Sheel, F.J.E. Bolton, H.A. Foster, Antimicrobial Activity of Novel Nanostructured Cu-SiO₂ Coatings Prepared by Chemical Vapour Deposition against Hospital Related Pathogens, *AMB Express* 3 (2013) 53, <https://doi.org/10.1186/2191-0855-3-53>.
- [68] S. Velho-Pereira, A. Noronha, A. Mathias, R. Zakane, V. Naik, P. Naik, A.V. Salker, S.R. Naik, Antibacterial Action of doped CoFe₂O₄ Nanocrystals on Multidrug Resistant Bacterial Strains, *Mater. Sci. Eng., C* 52 (2015) 282–287, <https://doi.org/10.1016/j.msec.2015.03.046>.
- [69] Y. Yan, C. Li, H. Wu, J. Du, J. Feng, J. Zhang, L. Huang, S. Tan, Q. Shi, Montmorillonite-Modified Reduced Graphene Oxide Stabilizes Copper Nanoparticles and Enhances Bacterial Adsorption and Antibacterial Activity, *ACS Appl. Bio Mater.* 2 (5) (2019) 1842–1849, <https://doi.org/10.1021/acsbm.8b00695>.
- [70] S. Zhang, J. Ye, Z. Liu, H. Lu, S. Shi, Y. Qi, G. Ning, Superior Antibacterial Activity of Fe₃O₄@Copper(II) Metal-Organic Framework Core-Shell Magnetic Microspheres, *Dalton Trans.* 49 (2020) 13044–13051, <https://doi.org/10.1039/DOTD02417A>.
- [71] J. Jiang, C. Ling, T. Xu, W. Wang, X. Niu, A. Zafar, Z. Yan, X. Wang, Y. You, L. Sun, J. Liu, J. Wang, Z. Ni, Defect Engineering for Modulating the Trap States in 2D Photoconductors, *Adv. Mater.* 30 (40) (2018) 1804332, <https://doi.org/10.1002/adma.201804332>.
- [72] L. Yin, P. He, R. Cheng, F. Wang, F. Wang, Z. Wang, Y. Wen, J. He, Robust Trap Effect in Transition Metal Dichalcogenides for Advanced Multifunctional Devices, *Nat. Commun.* 10 (1) (2019) 4133, <https://doi.org/10.1038/s41467-019-12200-x>.